Acknowledgements

Thomas Sowell once said, "It takes considerable knowledge just to realize the extent of your own ignorance." By this metric, I feel comfortable saying that grad school has made me a considerably more knowledgeable person. With that in mind, I would like to thank several (but by no means all) of the people who aided me along this path. First and foremost is my family, especially my parents. Without your seemingly endless patience and support, especially during my less-than-productive years of college, I would not have made it half as far as I have.

Austin Holland, I am grateful for having you as a mentor. Your patience and laissez-faire supervisory style allowed me to be creative, explore, and grow as a scientist. Your objectivity and impersonal approach to science, especially in frustrating situations is something I hope I learned from you. Dr. Keller, you were the one that got me interested in geophysics instead of geology in the first place. Despite being a busy, important person, you always took an interest in what I was working on and made the time to explain anything I needed help with. Dr. Elmore, thanks for letting me screw around in Pmag for a while, for recommending that I jump ship on my first topic, and for playing a large roll in getting me into grad school in the first place. Dr. Rich, while you were less involved in my research than the rest, conversations with you greatly shaped my expectations of life in academia and industry, which significantly impacted the choices I made about my future.

Several people volunteered their time to collect data that was either used in this thesis or on a previous thesis topic that did not come to fruition. The seismic data presented here was collected by many students, organized by Randy Keller, Steve Holloway, Austin Holland, and Kevin Crain; these students are Cullen Hogan, Derek Lee, Guang Chen, Hamed Al-Rafaee, Jefferson Chang, Jon Buening, Jon Green, Michele Xiaoyu, Xiao Xu and Xiaosan Zhu. I would like to thank Jessicat Tréanton (tu me manques) for selflessly giving up several days to go camping and drinking and visiting breweries for the sake of helping me collect rocks, Ali Stuellet for the field assistance, and Neil Suneson for the assistance in and advice about field areas. I would also like to acknowledge some of my friends for just being friends and making my time here a more positive experience: Angela, Bryan, Em, Jess, Rachel, Robert, Shawn, and many others (basically, if you're my friend, give yourself a half-hearted pat on the back for me – you've earned it).

The financial support of, and employment by the Oklahoma Geological Survey is something I am very grateful for, as well as the support and guidance of the School of Geology and Geophysics faculty and staff. I am also appreciative to both these departments for the opportunity to take part in, and present at several professional conferences.

I tell you, we are here on Earth to fart around,

and don't let anybody tell you different.

-Kurt Vonnegut

Table of Contents

List of Tables

List of Figures

Abstract

In this study we use a uniquely collected seismic dataset to investigate the shallow velocity structure of part of central Oklahoma. The dataset consists of eight earthquakes recorded on 156 vertical component 4.5Hz geophones that were deployed spanning two pockets of seismicity ~70km apart. A total of 24 sonic logs were digitized and used to construct an initial 1D velocity model. First arrivals for both P and S phases were picked and used to calculate initial hypocenters in the 1D model. The resulting travel-times were used to conduct an iterative source location/velocity inversion: A 3D tomographic model was inverted for, and this resulting 3D velocity model was subsequently used to relocate the hypocenters, which were then used to refine the earlier tomographic model. Two techniques verified that these few sources adequately constrained the inversion: First, the dataset was resampled several times so that the inversion was performed using only six randomly selected earthquakes instead of the full eight; Second, the dataset was expanded to include sources and receivers from the regional seismic network that had been operating in the area.

Several velocity anomalies were observed in the tomography on both the P and S velocity models. Negative Vp and Vs anomalies were resolved in the top 1 kilometer of the model. Strong negative Vp and Vs anomalies are also resolved between 3km and 7km depths in both of the seismic zones. The deep anomaly observed in the eastern source area expresses a more complicated structure in the Vp tomography than it does in the Vs tomography, while the deep anomaly in the western source area has the same expression in both the Vp and Vs inversions.

The consistency of these anomalies in the tomographic inversions using resampled datasets as well as an augmented dataset indicates that these anomalies are not merely artifacts. The correlation of the location of the velocity anomalies to gravity or magnetic anomalies further validates our tomographic models.

Due to the amplitude of these lateral heterogeneities and their correlation to potential field anomalies, we feel that hypocenters calculated in a 1D model cannot adequately represent the true distribution of seismicity in the study area. We use the final 3D velocity models to relocate over 100 of the Wilzetta Fault and Jones Swarm earthquakes that were observed at the greatest number of stations, finding that all of these events were located in the crystalline basement.

Chapter 1: Introduction

The earthquake tomographic inverse problem is underdetermined. This means that the amount of data required to unequivocally constrain the velocity at every node within a velocity model, as well as the precise hypocenter location, is never obtainable. This is because the exact temporal and spatial location of the energy source is unknown and must be solved for in an assumed velocity model, while the velocity model itself is also not explicitly known. Additionally, noise in the data, as well as the fact that the data is discretized, further complicates the modeling process by adding uncertainty to all measurements. Using absolute seismic arrival times, one must solve for both the slowness field and the hypocenter. One common approach, which we use here, is to derive a velocity model from sonic logs and find a "minimum 1-D model" (Kissing et al., 1994) in which to locate the earthquakes. From this starting minimum 1D model, tomographic inversion is then used to solve for anomalies in the derived velocity model.

In general, one of the difficulties in earthquake seismology is the fact that earthquakes are inherently unpredictable, both temporally and spatially. Long-term trends in seismicity, and correlations to geologic features may in time be established, but in intra-continental regions considered to be relatively quiescent, this becomes a challenge. Seismic monitoring networks in these environments are often limited too, consisting of only a few stations over a broad area. To compensate for the lack of instrumentation, temporary seismic monitoring stations are often used to fill in gaps in a region's seismic network (e.g. Kennett and Hilst, 1996). These temporary stations are often deployed in areas where seismicity rates are temporally elevated, which allows for a more in depth analysis into the nature and distribution of seismic swarms. However, even these temporary stations can be restrictively expensive, both for financial and logistic reasons, limiting the possible station coverage and the total number of stations that can be deployed.

In this study, we attempt to overcome some of the aforementioned financial and logistical limitations by using two pockets of increased seismicity, which are separated by ~70 km, as source regions for a passive tomographic survey using a dense, short-lived deployment of 156 inexpensive 4.5Hz vertical-component geophones, each coupled with a Ref Tek 125 “Texan” data logger. These receivers were deployed in two lines, an east-west line consisting of 123 units, and a north-south line consisting of another 33 units (Fig. 1). These lines intersect near the densest distribution of epicenters on the Wilzetta Fault Zone (WFZ), which was the site of the November 6th, 2011 **M**5.7 Prague earthquake and aftershock sequence (Fig. 2). On the east-west receiver line, the station spacing was generally 1km, but in the areas where we see the most seismicity, the spacing was reduced to 0.5km. Station-station spacing on the north-south line was ~0.5km. The Texans recorded continuously during four consecutive nights to minimize cultural noise, and captured 6 WFZ events and 2 Jones swarm events. Additional seismic networks were active in the study area at the time. The U.S. Geological Survey (USGS) and the University of Oklahoma (OU) deployed eighteen high-quality 3-component seismometers near the WFZ, and the data from these instruments were also included in the tomography.

1.1 Background

The study area is eastern Oklahoma County and southern Lincoln County in central Oklahoma (Fig. 1). In eastern Oklahoma County a diffuse zone of seismicity, referred to as the Jones swarm, began in 2008 (Keranen et al., 2014), but increased in activity mid-2009 and is still ongoing. The other seismic source, located in southeastern Lincoln County, was the aftershock decay sequence of the 2011 **M**5.7 Prague earthquake on the WFZ. At the time of the data collection (January 20-24, 2012), the 2011 WFZ aftershock sequence was still active (Fig. 2).

Several large geologic features are present in Oklahoma surrounding the study area on a regional scale (Fig. 3). To the west of the study area is the Nemaha Fault Zone and the Anadarko Basin; to the southeast are the Arkoma Basin and Ouachita Mountains; to the south, the Arbuckle Mountains; and to the southwest, the Wichita Mountains and Southern Oklahoma Aulacogen (Northcutt and Campbell, 1995). However, the majority of central Oklahoma, where this study took place, bears little evidence of tectonic complexity at the surface. Huffman (1958) found a 1° westerly dip due to the Ozark uplift in east of the study area, but the subsurface dip increases significantly towards the Nemaha fault to the west (Johnson, 2008). Additionally, several subsurface faults in and near the study area on the Cherokee Platform have similar orientations (Fig. 3) including the Wilzetta Fault, White Trail Fault, Keokuk Fault, Wewoka Fault, Weleetka Fault, and East Mountain Fault System (Toelle et al., 2008).

1.2 Previous Work

Previous studies investigating the crustal structure of central Oklahoma are few in number. Tryggvason and Qualls (1967) conducted a reversed-refraction profile from Chelsea in northeastern Oklahoma to Manitou in southwestern Oklahoma, deriving a 1D velocity model down to ~50km. Mitchell and Landisman (1970) revisited this dataset, developing a 2D velocity model. However, even though the profile line in these studies passes through the western side of our study area, both of these studies were focused on a much larger scale than the present study, so the final models lack resolution relevant to this study. An integrated geophysical study was conducted by Elebiju et al. (2011) in Osage County, in an area that is ~150km northeast along strike of the Wilzetta Fault. This study revealed several seismic reflectors in the basement that indicated that the basement rock in Oklahoma could have significant lateral velocity heterogeneity.

Both of the seismic source regions have received some attention, but the Jones swarm has not been the target of as much research as the WFZ sequence has; this is likely do to the fact that the WFZ has produced higher-magnitude earthquakes than the Jones swarm. Holland (2013) found that the focal mechanisms for the Jones swarm were more consistent with the orientation of naturally open fractures in the crystalline basement than with focal mechanisms observed throughout the rest of the state. It was also found that the b-value in the Jones area was distinctly different than that of the rest of Oklahoma, indicating that the cause of the Jones swarm was likely different from the rest of the seismicity in

Oklahoma. Keranen et al. (2014) proposed that the Jones swarm is induced by fluid pressure from high-rate disposal wells located ~20km to the southwest, and that the injection fluid pressure migrates up-dip towards the Jones swarm.

A few previous studies have investigated the structure of the WFZ in the study area, most notably is Dycus (2013) who expanded on previous studies (e.g. Joseph, 1986; Way, 1983) by incorporating additional well control, considering regional structures and stresses, structural kinematics, and earthquake focal mechanisms. Dycus (2013) reports a previously undocumented fault in the WFZ, mapped from hypocenters in the 2011 WFZ aftershock sequence ("Meeker-Prague Fault", Fig. 1).

The recent seismicity of the WFZ has also been investigated. Keranen et al. (2013) reported locations for the earthquakes that occurred during the first week of the 2011 WFZ sequence, finding that 20% of the earthquakes were located in the sedimentary column, namely the Arbuckle Group into which wastewater is being injected, with the remainder occurring in the crystalline basement. Additionally, Keranen et al. (2013) proposed a hypothetical model explaining how the Prague earthquake sequence could be explained via induced seismicity. However, it should be noted that their proposed model used arbitrary modifications to the 30-year-old structural map of Way (1983), and lacked the data to properly test their hypothesis. van der Elst et al. (2013) found that transient stress perturbations generated by strong, distant earthquakes likely triggered the WFZ seismicity. Sumy et al. (2014) derived the Coulomb stress change for the three largest earthquakes in the WFZ sequence, showing that these events increased local Coulomb stress, thereby promoting additional fault failure.

Chapter 2: Methods

2.1 Initial Model Generation

The first step in this study was to generate a minimum 1D velocity model for the Jones-Prague study area. Although Keranen et al. (2013) derived a velocity model for their study, for several reasons we derived our own model: 1) the Keranen model was based off of only two sonic logs whose locations were not reported; 2) Sonic logs only reach a maximum of 1.5km below mean sea level (MSL), and it was not reported if and how their model was constrained at depth; and 3) a comparison of the Keranen model to the available sonic logs (Fig. 4) suggested that we could obtain a better fit to the *a priori* data.

A total of 24 sonic logs near the WFZ were digitized and averaged, and were then used to generate an *a priori* 1D velocity model down to ~2.0km below MSL. Robert Herrmann (personal communication, 2012) analyzed surface wave dispersion curves to generate a velocity model to a greater depth (~80km). From these two independently derived velocity models, both gradient-based and discrete-layer Vp and Vs models were derived for use this study. The sedimentary/crystalline-basement interface was approximated as 2.0km below MSL; this value is the approximate depth to crystalline basement near the WFZ (Luza and Lawson, 1983) and was also used as the top of basement in Keranen et al. (2013).

The *Seisan* software package (Havskov and Ottemöller, 1999) was used to pick 1059 P wave first arrivals and 619 S wave first arrivals, and was then used to calculate initial hypocenters in the 1D *a priori* model. *Velest* (Kissing et al., 1994) is an inversion program that modifies a 1D velocity model and hypocenters to obtain a "minimum 1D model." The velocities and hypocenters are adjusted to minimize the misfit between the initial 1D velocity model and the observed travel times for a given set of earthquakes. This program was used to solve for minimum 1D model from the *a priori* model and the eight well-recorded earthquakes (discrete-layer models in Figs. 4 and 5).

2.2 Tomography

The *FMTomo* software (Rawlinson et al., 2006), referred to here as FMT, was used to conduct the 3D tomographic inversion. FMT was chosen over other 3D tomographic software for several reasons: 1) it treats the tomographic inverse problem non-linearly which seemed advantageous given the high-density of the station spacing in this study; 2) the code is highly modularized so we could be selective about which routines were being integrated into our analysis approach, which was necessary for the highly-customized processing scheme used here; and 3) options for generating checkerboard models and synthetic datasets are included in the software package. FMT uses a fast-marching technique to forward model travel-times in a 3D medium, and then uses a subspace inversion scheme to adjust the velocity model to accommodate the travel time residuals.

Even though FMT contains a routine for source inversion, a joint hypocenter/velocity inversion did not perform stably when using only 8 sources.

NonLinLoc (Lomax et al., 2000), herein referred to as NLL, was the primary program used to locate the hypocenters. NLL uses an iterative 3D grid-search routine that uses successively finer grids to find a probability density function for hypocenter locations. Initial locations for the tomographic inversion were generated with NLL in the minimum 1D model.

Since NLL has ability to locate earthquakes in complex 3D velocity models, we used a shared 3D velocity grid between FMT and NLL, where the grid spacing is 1km in all directions. The velocity model after tomographic inversion would become the velocity model in which NLL would relocate hypocenters. Using this new set of hypocenters, the tomography would be repeated. Thus, we developed an iterative 3D hypocenter location and tomography procedure (Fig. 6).

As previously mentioned, the tomography problem is underdetermined. To mitigate this problem, tomography packages use various inversion parameters to control how the velocity model is modified to fit the data. Specifically, FMT uses a "damping" and a "smoothing" parameter. The damping parameter affects the magnitude of the velocity adjustment applied to individual velocity nodes, and the smoothing parameter acts as a filter, preventing individual velocity nodes from being adjusted significantly more than surrounding nodes. In tomography, the optimal inversion parameters are often found through grid searching or trade off curve analysis, but in this study, we over gridded the velocity grid so that the *a priori* data and dense receiver spacing could be better honored. Standard inversion optimization techniques in this set-up would therefore lead to under-estimated inversion parameters and an excessive amount of short-wavelength anomalies. Instead, we performed a grid search for optimal inversion parameters in a more appropriately gridded velocity model. Using the size and amplitude of the resulting velocity anomalies in the optimized inversion as a guide, we back-solved via trial-and-error for the appropriate damping parameters in the over-gridded models.

2.3 Model Validation

Checkerboard resolution tests are used to assess the minimum size velocity anomaly that can be imaged with a given source-receiver configuration. They work by incorporating alternating high and low velocity anomalies throughout a velocity model, generating a synthetic dataset in this geologically unreasonable model, and then using this synthetic dataset in a layer-cake model to attempt to recover the checkerboard anomalies via tomographic inversion. For the checkerboard resolution test used to access the imaging capability of our survey configuration, velocity perturbations of ±0.5km/sec were incorporated into the otherwise layer-cake Vp model and ±0.3km/sec anomalies in the Vs model. Several checkerboard tests were conducted, varying the anomaly size from 2km to 20 km.

While the checkerboard test is useful in determining the possible resolution in a tomographic survey, it assumes that the locations of the energy sources are absolutely known. This is never the case with earthquakes, and because this survey uses a small number of events recorded on a denser receiver network than what is typically used in passive seismology, we must evaluate the model uncertainty. To this end, we performed a jackknife analysis of our dataset following Tichelaar and Ruff (1989). Of the 28 possible combinations of 6 earthquakes, seven combinations were randomly generated and used in the iterative inversion/relocation scheme shown in Fig. 6. The results of these inversions were used to calculate an average velocity model and the level of certainty through the model, expressed as the standard deviation of the jackknifed models. To further understand how the jackknifed models differ individually, we calculated the mean absolute percent difference (MAPD) for each of the final tomographic models generated with a jackknifed dataset using the following equation:

$$MAPD = \sum_{v=1}^{n} \left| \frac{R_v + B_v}{R_v} \right| \qquad (1)$$

In this equation, *Rv* is the velocity at a node in the model generated from all 8 earthquakes (hereafter referred to as the reference model), *Bv* is the velocity at the same node in the jackknifed model, and the summation is over *v*, all the velocity nodes in the seismic volume.

To further investigate the limitations of only having eight sources in this tomographic dataset, we generated another dataset by augmenting the eight well-recorded earthquakes with events recorded from the Oklahoma Geological Survey's (OGS) regional seismic network as well as the additional 18 OU and USGS seismographs near the WFZ. The OGS operated five USGS NetQuakes in the study area, two in the Jones swarm and three in the WFZ. The NetQuakes instruments were the only additional instruments present on the Jones side of the model, and since they only record data when a minimum ground acceleration is reached, phase arrivals were only picked for Jones events where **M**>2.5 and Prague events where **M**>3.5. These magnitude thresholds were found to be the cut-off at which the NetQuakes would record earthquakes. We only added data during the period that the 18 OU and USGS stations were deployed (Nov. 6th, 2011 – Mar. 7th, 2012) to ensure that the inversion only used well-constrained hypocenters. This resulted in an additional 17 earthquakes in the Jones swarm and 12 earthquakes in the Prague sequence being added to the analysis. This augmented dataset consisting of the 8 primary earthquakes and the additional 29 earthquakes was then used in the iterative inversion/relocation scheme depicted in Figure 6.

The tomographic results were also compared to available gravity and magnetic data. The gravity and magnetic data was acquired from the Pan American Center for Earth and Environmental Studies located at the University of Texas and El Paso, and from a prior OGS gravity survey in the study area. While the tomographic data is primarily restricted to a single line of geophones, the gravity and magnetic data show how the final inversion models may correlate to broader geophysical anomalies.

Chapter 3: Results

The minimum 1D velocity model derived here differs appreciably from that of Keranen et al. (2013), whose model includes a 3km/sec discontinuity in the shallow sedimentary column and is as much as 1km/sec too slow immediately above the formation into which wastewater is being injected (Figs. 4 and 5). Their model is also generally slower in the top 1.5km of the sedimentary column than what the sonic logs show, which would cause hypocenters to artificially be calculated to a shallower depth than they should be. The locations of the eight well-recorded earthquakes used here are shown in Table 1, and have an average RMS misfit of 0.07sec. While Keranen et al. (2013) found that 83% of the seismicity in their study was <5km deep, this small sample of well-constrained earthquakes shows a deeper trend.

Checkerboard resolution tests show that the minimum size velocity anomaly capable of being resolved in the top 4km of the model and in the immediate vicinity of the sources is ~5km in both the P and S velocity inversions (Figs. 7 & 8). However, features were only resolvable on the E-W densely instrumented line. The ~12 km long N-S line was not long enough to resolve any anomalies, and because most the sources are at approximately the same latitude, there was minimal ray crossing. Broader structures were partially resolved in the center and deeper portions of the model, as shown in Figures 9 and 10, which show the recovery 20km x 20km anomalies for the P and S models, respectively. The geometry of the recovered anomalies varies slightly from that of the initial anomalies because of the smoothing parameter in FMT, which restricts the inversion from recovering abrupt velocity discontinuities. It should also be noted that the checkers used in the resolution test were 3D features, and because this study relies heavily on a single line of instruments, it is possible for the inversion to partially bend rays around anomalies instead of fully resolving them. Conversely, it is possible that long, continuous features that intersect the main instrument line (e.g. the Wilzetta Fault or changes in basement lithology) can be resolved to a finer degree than what the checkerboard test suggests. Since the checkerboard pattern FMT incorporated into the model is not smoothed, the resolved checkerboard also shows us the maximum velocity gradient the inversion can image.

Due to the geometry of the receiver deployment, and as indicated by the checkerboard tests, the results of the inversion are best constrained under the east-west geophone line. Since this instrument line had earthquakes located at both ends, it effectively simulated a reversed refraction profile. The north-south geophone line and the scattered deployment of broadband seismometers help to constrain hypocenters by enhancing the azimuthal coverage, but do not contribute as much to the tomographic effort due to the locations of the seismic sources. Consequently, most of the discussion and figures focus on a latitudinal cross section at 35.55°N.

Using the main dataset of 8 earthquakes, the initial model misfit between the P arrivals and the minimum 1D velocity model is 393ms, and for the S arrivals it is 470ms. During inversion using the hypocenters located in the minimum 1D model, the travel time misfit for the P velocity model converged to 111ms (Fig. 11), and 162ms for the S velocity model (Fig. 12). Using hypocenters calculated in the inverted S and P velocity models shown in Figures 11 and 12, the inversion residuals were further reduced to 98ms for the P model (Fig. 13), and 142ms for the S model (Fig. 14). Figures 15 and 16 show the changes that were made to the 1D inversion model after the relocation of earthquakes in the 3D medium. Additional iterations through the relocation/re-inversion scheme were conducted;

however, model convergence did not improve by more than 1% after the first tomographic inversion that used hypocenters located in previously generated 3D velocity models.

The results from jackknifing the dataset were very similar to that of the inversion using all eight events. The average velocity models (Figs. 17 & 18) differ very little from the reference models (Figs. 12 & 14). The standard deviation of the Vp models (Fig. 17) shows the greatest uncertainty below the WFZ events where we do not actually have ray coverage. In the remainder of the model, the standard deviation rarely exceeds 0.15km/sec. The results of jackknifing the Vs data show that the velocity uncertainty seldom exceeds 0.1km/sec. The MAPD for all the jackknifed P velocity volumes varied between 1.3% and 2.2%, and for the S velocity models the variations were between 0.6% and 1.5%. Figures 19 and 20 show the final inversion model and MAPD for the P and S velocity inversions that differed the most from the reference model. The level of consistency across these models shows that our inversion was well constrained, and that we can have high confidence in areas of the model that checkerboard testing was successful.

Similar models were recovered using this process on the augmented dataset. The most notable differences are that in the Vp model (Fig. 21), the WFZ low-velocity anomaly has lower amplitude, and the Jones low-velocity anomaly has higher amplitude. In the Vs model (Fig. 22), these differences are not present, and the final model is extremely similar to the results of the inversion using only the 8 well-recorded earthquakes. The MAPD calculated between the augmented dataset and the reference model fell within the range of the MAPD values from the jackknifed datasets. For the P velocity model, the difference was 1.7% (Fig. 21) and for the S velocity model it was 1.2% (Fig. 22).

We selected ~100 of the earthquakes in the 2011 Wilzetta Fault rupture sequence that were observed on the greatest number of stations. Data from the 18 temporary OU and USGS instruments are included in this dataset, as well as observations from the OGS regional seismic network. Seventeen events in the Jones swarm were also included. Few Jones events were included because, as discussed earlier, the instrumentation in the Jones area was sparse, and the instruments that are nearest are NetQuakes accelerometers, which only record data above a minimum ground motion threshold. This set of earthquakes was relocated in the velocity models constrained from the 8 well-recorded earthquakes, and the locations are shown in Figure 23 and reported in Table 2. NonLinLoc reports hypocenter uncertainty as 68% confidence ellipsoids around calculated hypocenters. For this dataset, the average vertical uncertainty was 40m. The horizontal uncertainties were, on average, 13.5m and 8m on the semi-major and semi-minor axes, respectively. None of these hypocenters were located above 2km below MSL, which, for the WFZ, is the assumed interface between crystalline basement and the sedimentary column in both this study and Keranen et al. (2013).

Finally, a Vp/Vs cross section was generated from the final P and S velocity models (Fig. 24). The Vp/Vs model shows a general low Vp/Vs ratio (~1.65), as well as some local variations. Very low Vp/Vs ratios, as low as 1.45, are observed in the shallowest portions of the model. While these low ratios are below what is generally considered reasonable for typical lithologies, previous studies (e.g. Brocher, 2008) have found that these low Vp/Vs ratios can be found in shallow sediments. The most intense Vp/Vs variations, however, are smaller than the 5km resolution limit indicated by the checkerboard tests, and are located in areas of the model where the jackknifing indicated higher uncertainties.

Chapter 4: Discussion

Reprocessing the hypocenters in the 3D model, and refining the 3D models in FMT with these new hypocenters decreased traveltime misfit by ~10% in the first iteration. Additional iterations resulted in trivial (~1%) changes to the model, and did not always reduce misfit. This model refinement affected the velocities at depths typically less than 4km. In general, the velocities were decreased, where they changed at all, during the refinement. Jackknifing the dataset yielded faster velocities in the top 4km of the models, but slower velocities in the low-resolution zone between the source regions (Figs. 19 and 20). Inversion of the augmented dataset yielded more complex distribution of minor changes (Figs. 21 and 22). The strongest change in the augmented inversion over the reference model was that the inversion using many more events in the Jones swarm yielded slower velocities in the Jones hypocentral area. However, the USGS NetQuakes instruments, which were the only additional instrumentation near the Jones swarm, have a lower temporal resolution than any other instrument used in this survey.

Figure 25 shows the recovered velocity structure under the main geophone line with added labels for the velocity anomalies. In the very shallow subsurface, three low Vp and Vs anomalies are present. The two near the Jones swarm, referred to here as anomalies A and B, correlate with where the Canadian River intersects the main geophone line, and the one located on the east side of the model, anomaly C, is over the Wilzetta Fault. Smaller perturbations are present but are below the 5km resolution limit indicated by the checkerboard testing and are therefore ignored in our analysis. Two deeper, larger low velocity anomalies are resolved, one in the Jones swarm source area (anomaly D) and one in the WFZ (anomaly E) in both the Vp and Vs models. Anomalies A-D are roughly the same shape and intensity in both the Vs and Vp models. However, in the Vp model anomaly E has higher amplitude, is broader, has higher velocity gradient at its boundaries, and has a small high-velocity anomaly contained within the overall lower velocity structure. While this minor high-velocity is below the resolution threshold indicated via checkerboard testing, it's presence in the tomographic models generated from the jackknifed datasets (Figs. 17 and 19) as well as the augmented dataset (Fig. 21) suggest that this may be evidence of further complexity in the velocity structure of the WFZ.

Maps of the gravity and magnetic fields were also compared to the tomographic results. Minimal processing was done on these datasets in Geosoft's *Oasis Montaj* software package. The magnetic anomaly map was reduced to the magnetic pole (RTP) and the results are shown in Figure 26. For the gravity field data, the Bouguer anomaly map was upward continued to 5km, a process that effectively acts as a low-pass filter, and this upward-continued map was subtracted from the original Bouguer anomaly map. The resulting residual map (Fig. 27) thus omits longer wavelength regional trends and depicts the local variations in the gravity field.

The gravity trend along the main receiver line, as shown in Figure 27, is generally increasing to the east, as the basement becomes shallower (Luza and Lawson, 1983). Since crystalline basement is denser than sedimentary rock, this correlation of gravity to the depth to basement is to be expected. The exception to this trend is a slight dip in gravity around the WFZ that is collocated with anomaly E, which also correlates to a slight positive anomaly on the RTP map (Fig. 26), a high Vp/Vs ratio at depth (Fig. 24), and a decrease in Vp and Vs in all the tomography inversions (e.g. Fig. 25). One of the strongest features seen in the potential fields is a negative anomaly, labeled F, on both the gravity and RTP maps. Due to the limits of the survey geometry, the inversion using only 8 events did not have rays passing through this area. However, the augmented dataset had a receiver and sources in that area, and consequently, anomaly F is emerges in the tomography using this dataset (Fig. 28).

A map of basement lithologies in central Oklahoma is shown in Figure 29. The lithologies were determined from the 56 basement-penetrating wells in the mapped area, and the lithological contacts were interpreted from regional gravity and magnetic data by Denison (1981), who interpreted two basement lithologies in our study area: the 1.28 Ga Central Oklahoma Granite Group and the 1.28 Ga Spavinaw Granite Group. However, since none of the basement-penetrating wells used to constrain the map of basement lithologies were located in our study area, we use the velocity and magnetic anomalies in the tomographic model to constrain a re-interpretation of the basement lithology changes (Fig. 26).

Figure 30 shows a block model of the study area, comparing the RTP magnetic map to the Vp cross-section. On the west side of the model, anomaly D correlates with a basement lithology change mapped by (Luza and Lawson, 1983), with the lower velocity and higher magnetization correlating with the Central Oklahoma granite group and the faster lithology correlating with the Spavinaw granite. In the WFZ, the velocities are higher on the east side of the fault projected to a greater depth, which is consistent with the interpretation of Dycus (2013) that, in this area, the east side of the Wilzetta Fault is up thrown. Since anomaly D and E are similar in that they are associated with low velocities and high magnetizations, one possible explanation for the low velocity in the WFZ would be a change in basement lithology, similar to anomaly D. Due to the lack of ray coverage (Figs. 13 and 14) on the east side of anomaly E and the west side of anomaly D, it is unknown if the velocities truly increase along the edges of the models as shown (Fig. 28).

The consistency of the anomalies in all the geophysical models presented here further supports the validity of the tomographic results. However, one known feature that is not clearly recovered by the inversion is the known westward dip of the crystalline basement, which accounts for a depth-to-basement change of ~1km (Luza and Lawson, 1983). Conventional wisdom is that checkerboard tests are used to reveal the smallest resolvable structure, and any larger structures are going to be resolved as well. Lévêque et al. (1993)

demonstrated that this was not necessarily the case, and that sufficiently large features may not be imaged even if smaller features are. It may also be the case that the dip of the basement is too shallow to be resolvable in the tomographic inversion.

Chapter 5: Conclusions

Whether the 2011 **M**5.7 Wilzetta Fault rupture sequence was natural or induced, misidentifying its cause carries significant ramifications. If this episode of seismicity were to be falsely determined to partially be a product of human activities, then one of the strongest recorded earthquakes to have occurred in intra-continental North America would be omitted from seismic hazard assessment by the USGS. Conversely, if the seismicity were incorrectly determined to be natural, then the largest induced earthquake would be omitted from our understanding of the risks of subsurface fluid injection. Extra diligence must therefore be paid when it comes to identifying the nature of this seismicity, which begins with generating accurate velocity models of the subsurface and locating hypocenters in these models.

Based on the tomographic investigation, our study shows that the velocity structure in central Oklahoma may contain more lateral heterogeneity, similar to northern Oklahoma (Elebiju et al., 2011), than has previously been considered. The presence of these anomalies is further evidenced by their correlation with gravity and magnetic anomalies, and the consistency between jackknifed and augmented datasets. Due to the significance of the WFZ seismicity and the fact that these velocity anomalies are not of trivial magnitude, we feel that it is necessary to locate the seismicity in this region in 3D velocity models when available. By locating the earthquakes in 3D tomographic models, we found that the hypocenters are located shallower than they were in the minimum 1D model by as much as 1.4km, and that the average horizontal shift in location was 0.69km.

Despite the earthquakes being located shallower in the 3D model than in the 1D model, we find that the seismicity is still generally occurring deeper than what has previously been reported Keranen et al. (2013). The lack of hypocenters in the sedimentary column, and the recent structural mapping by Dycus (2013) are inconsistent with the model proposed by Keranen et al. (2013) citing reservoir pressure within a fault-bounded block in the Arbuckle Group as triggering the WFZ aftershock sequence. However, since their analysis only focused on the first few days of seismicity, whereas ours focused on earthquakes large enough to be observed through our entire study area, the datasets, and therefore the results, may not be directly comparable.

Despite the success of this experimental dataset and processing approach, the experimental survey design used here should be modified before being used again in the future. Due to the potential for earthquakes to occur at a substantial distance from densely spaced receivers, 3D tomography is required to accurately process the resultant dataset, and therefore a broader, more grid-like distribution of receivers should be used in the future. Furthermore, since there will always be inherent uncertainty in earthquake locations, and that the checkerboard testing showed that the smallest resolvable feature was ~5km, the station-station spacing of 0.5km in areas was unnecessarily dense. While additional stations are useful in the source areas to constrain hypocenters, the highly clustered nature of the seismicity minimized the number of crossing rays, thereby minimizing the resolving power of the tomography. Therefore, a broader, grid-like distribution of receivers would have produced better results.

Location in 1D models			Location in 3D models			Change in locations		
Depth (km)	Lat (˚)	Lon (˚)	Depth (km)	Lat (˚)	Lon (˚)	Depth (km)	Lat (km)	Lon (km)
5.107	35.5294	96.78461	4.343	35.5323	96.78641	0.764	0.283	0.176
6.743	35.5283	96.77209	5.357	35.5239	96.77701	1.386	0.430	0.481
8.404	35.533	96.78641	7.307	35.5254	96.79019	1.097	0.742	0.369
7.457	35.5327	96.76501	6.255	35.5274	96.76941	1.202	0.518	0.430
5.457	35.5592	97.28	5.251	35.5502	97.28079	0.206	0.879	0.077
5.757	35.5784	97.29541	5.393	35.5719	97.2981	0.364	0.635	0.263
4.457	35.5553	96.75339	4.253	35.5498	96.75562	0.204	0.537	0.218
5.743	35.5296	96.76941	5.007	35.5252	96.7774	0.736	0.430	0.780

Table 1: Hypocenter locations of the primary 8 events, showing the difference between the locations in minimum 1D models and final 3D tomographic models. The average horizontal change is 0.69km, and all earthquakes relocated shallower in the 3D model.

Depth (km)	Latitude	Longitude
3.11	35.5325	-97.0298
9.25	35.5821	-97.0528
4.46	35.5301	-96.7684
5.19	35.5302	-96.7957
9.74	35.498	-96.8682
5.74	35.5394	-96.8145
4.10	35.5489	-96.7874
5.46	35.535	-96.7994
6.44	35.5194	-96.8342
5.26	35.5312	-96.7703
5.46	35.516	-96.8657
6.29	35.5065	-96.855
4.74	35.553	-96.7925
4.80	35.5267	-96.8566
6.46	35.504	-96.8661
2.46	35.543	-96.7976
4.94	35.5232	-96.8468
6.26	35.5151	-96.8674
4.10	35.5171	-96.8036
4.74	35.5202	-96.8597
4.10	35.5183	-96.7831
6.10	35.5056	-96.8211
6.10	35.4921	-96.859
5.24	35.5082	-96.809
2.74	35.5106	-96.7927
4.20	35.5068	-96.7981
3.41	35.5122	-96.8023
3.10	35.4963	-96.8597
5.89	35.5132	-96.7867
4.74	35.5204	-96.7898
6.21	35.5593	-97.2856
4.74	35.5157	-96.7901
7.10	35.5325	-97.2744
3.01	35.5221	-96.7825
7.10	35.5348	-97.2802
3.46	35.4866	-96.8485
3.91	35.5055	-96.8162
3.74	35.4726	-96.7615
5.10	35.5275	-96.7779
3.84	35.4734	-96.7664
4.79	35.519	-96.8028

4.00	35.5234	-96.7775
4.45	35.5169	-96.7965
4.10	35.5431	-96.769
3.79	35.5197	-96.7864
3.10	35.5134	-96.7954
5.74	35.5249	-96.7879
3.76	35.4752	-96.7611
4.74	35.5276	-96.7727
6.10	35.5418	-96.7636
5.46	35.528	-96.7795
3.74	35.5246	-96.78
7.74	35.5447	-97.2817
3.74	35.4749	-96.8738
3.74	35.476	-96.8725
3.74	35.4743	-96.8759
8.10	35.5057	-97.2772
3.10	35.5118	-96.8017
3.04	35.5143	-96.7885
4.85	35.5282	-96.7793
3.96	35.5297	-96.7614
3.89	35.5339	-96.7736
3.74	35.4827	-96.8667
5.86	35.5296	-96.7841
5.01	35.5202	-96.7953
5.34	35.5168	-96.8043
5.74	35.5114	-96.814
5.74	35.532	-96.778
5.81	35.5294	-96.7821
5.74	35.5095	-96.771
3.75	35.4734	-96.9015
3.10	35.5504	-96.7569
3.74	35.4685	-96.7637
3.74	35.505	-96.8177
3.74	35.4746	-96.764
4.19	35.5177	-96.8023
7.74	35.5256	-96.7916
4.06	35.5169	-96.7987
3.41	35.4989	-96.8171
5.91	35.6126	-97.2299
6.91	35.5595	-97.299
7.74	35.5413	-97.2843
7.34	35.5271	-96.7846

2.19	35.5149	-96.8002
2.14	35.5183	-96.7832
3.10	35.5415	-96.7666
7.91	35.6122	-97.1997
3.10	35.5437	-96.7629
3.10	35.5096	-96.7685
2.10	35.5618	-96.7759
3.10	35.5039	-96.8235
2.46	35.5759	-96.779
7.74	35.5405	-97.2848
4.46	35.5211	-96.7896
4.45	35.4934	-96.8824
5.46	35.4895	-96.8897
3.10	35.5045	-96.7754
6.35	35.5889	-97.0586
6.96	35.5412	-97.2834
10.14	35.4317	-96.6819
3.10	35.5149	-96.802
3.10	35.5258	-96.7805

Table 2: Hypocentral locations for best-observed WFZ and Jones events relocated in the 3D reference models.

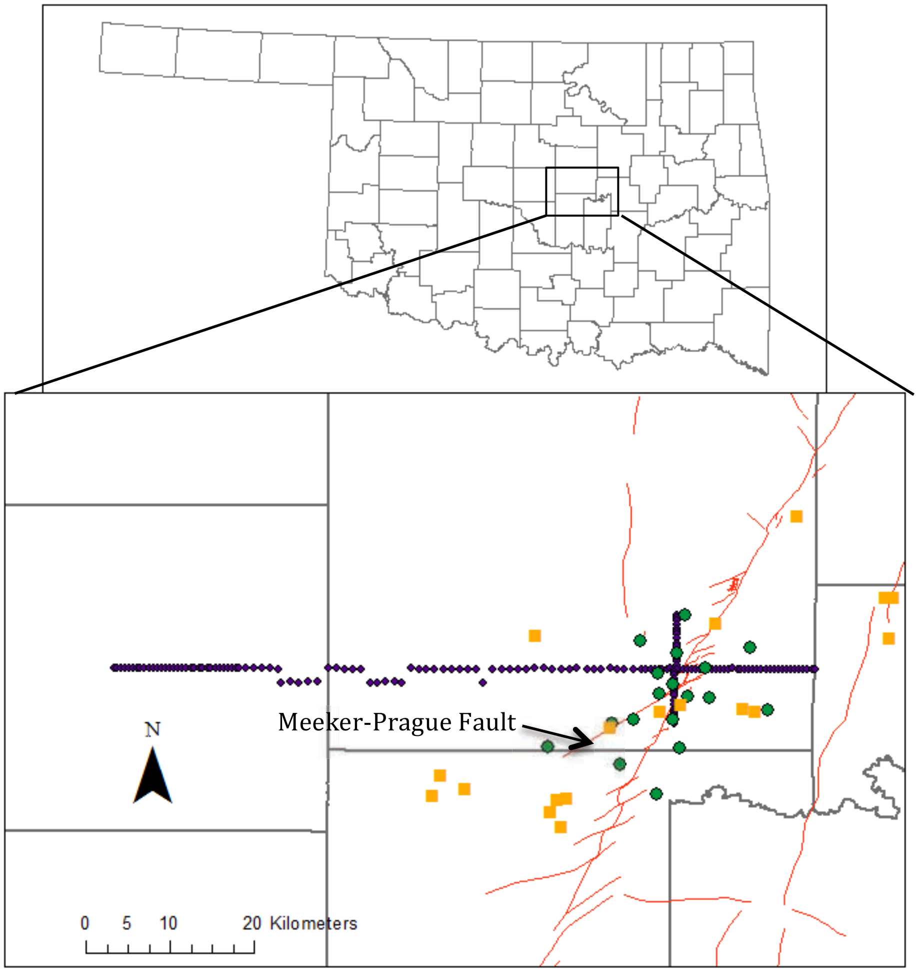

Figure 1: Map of study area in central Oklahoma. Orange dots are locations of sonic logs, green dots are locations of temporary broadband stations, purple dots are locations of geophones, and red lines are subsurface faults mapped by Dycus (2013).

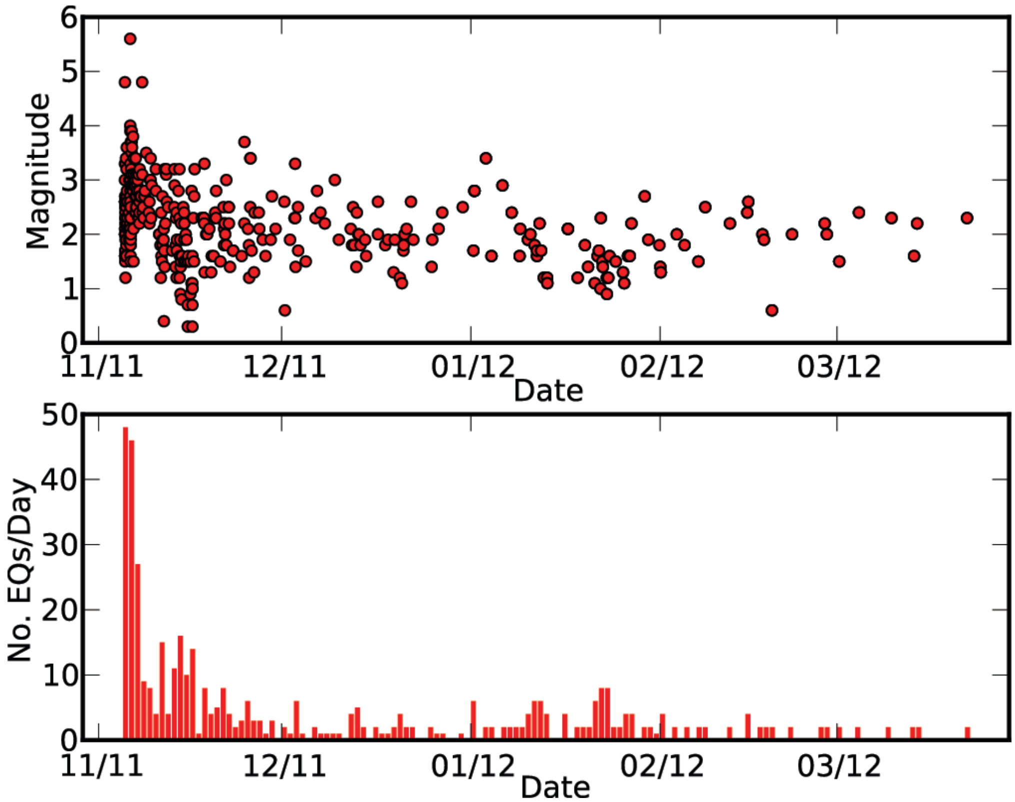

Figure 2: Top: Plot of magnitudes vs. time for the WFZ aftershock sequence between Nov. 11, 2011 and Mar. 31, 2011. **Bottom**: Plot showing the number of earthquakes per day against time for the WFZ aftershock sequence for the same period. At the time of the seismic data acquisition (January 20, 2012 through January 24, 2012), the 2011 **M**5.7 WFZ aftershock sequence was still active.

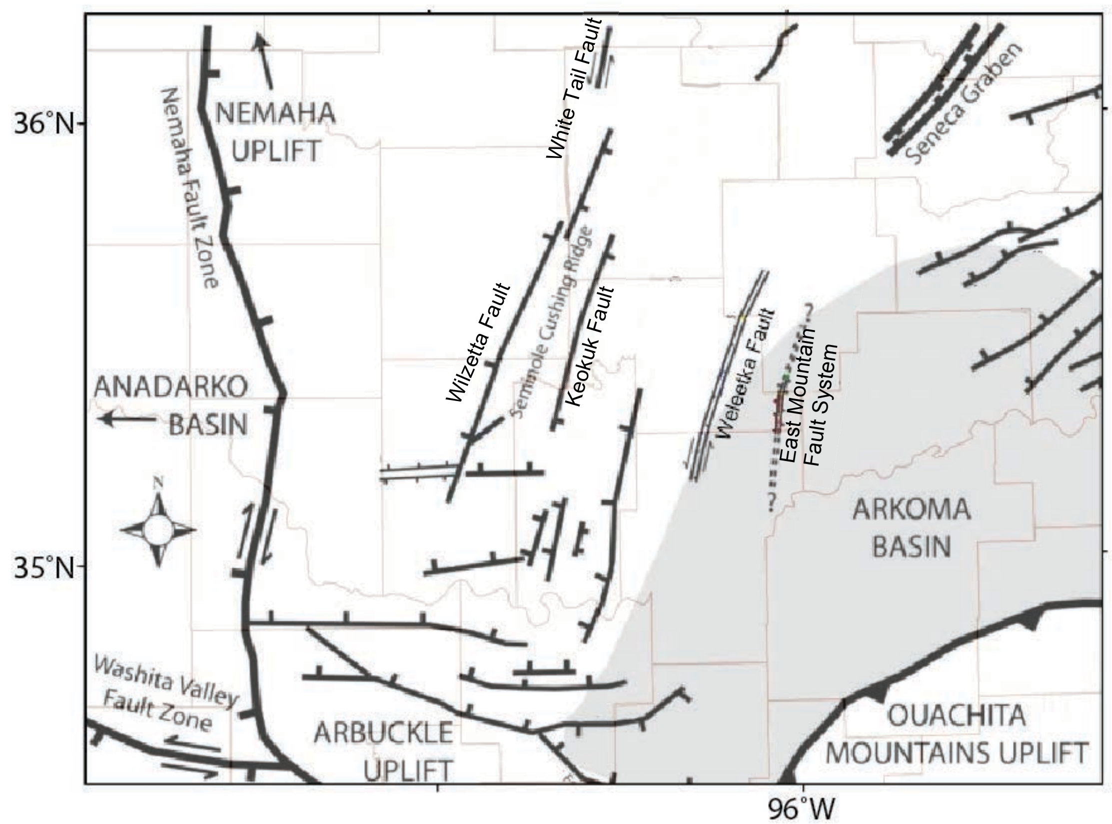

Figure 3: Mapped subsurface faults of central Oklahoma (Modified from Dycus, 2013) showing subparallel strikes. Several of the regional geologic features are also labeled.

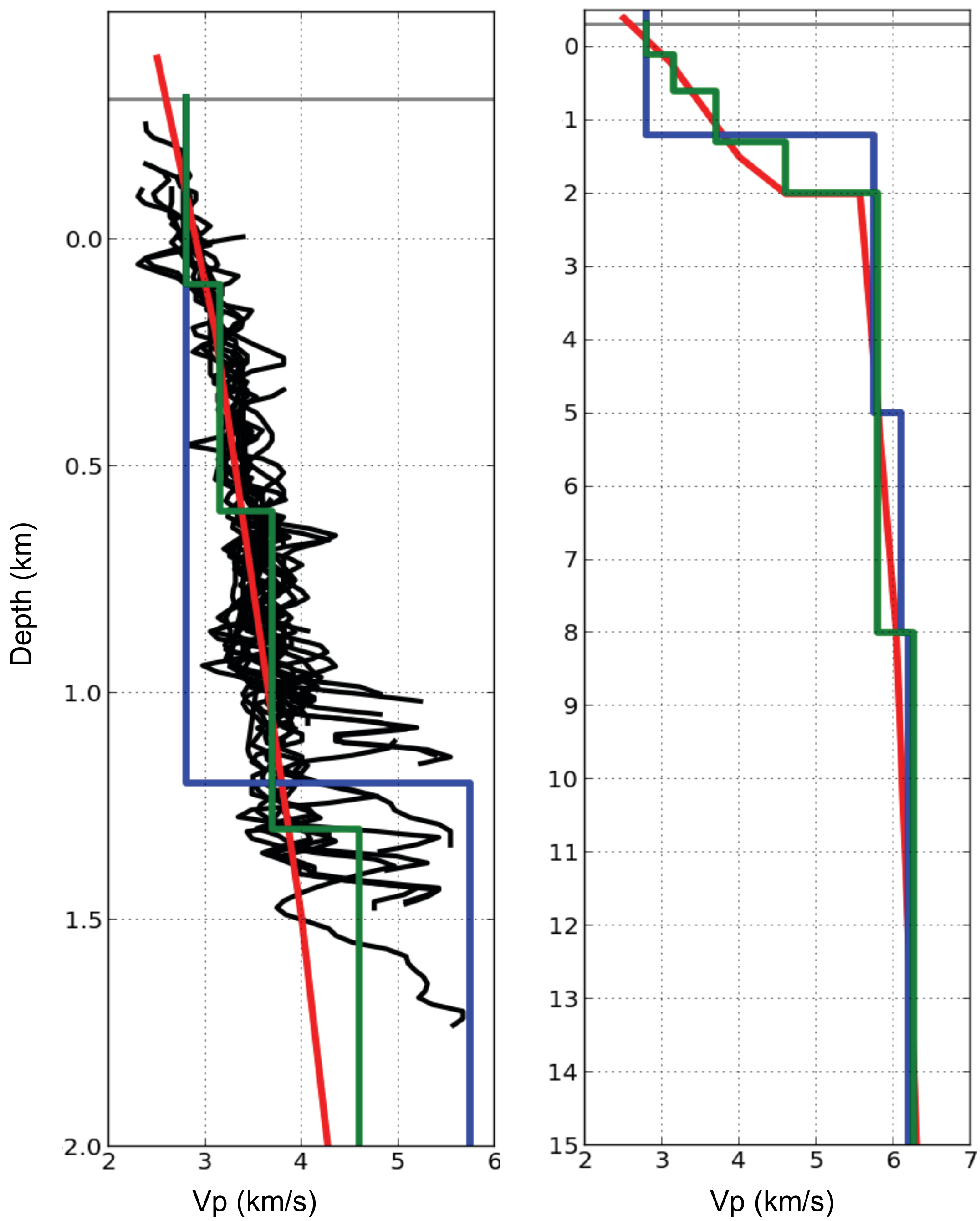

Figure 4: Left: Vp models and sonic logs from the Wilzetta Fault area down to 2km deep, the top of crystalline basement (Luza and Lawson, 1983). High-velocity noise in the sonic logs is likely an artifact due to wellbore instability. **Right:** Velocity models down to 15 km. *Blue*: final 1D model used in Keranen et al. (2013); *Red*: gradient-based starting model used in this study (input for NonLinLoc); *Green*; Minimum 1D discrete-layer starting model generated with Velest and used in this study (input for FMTomo); *Black*: Smoothed sonic logs.

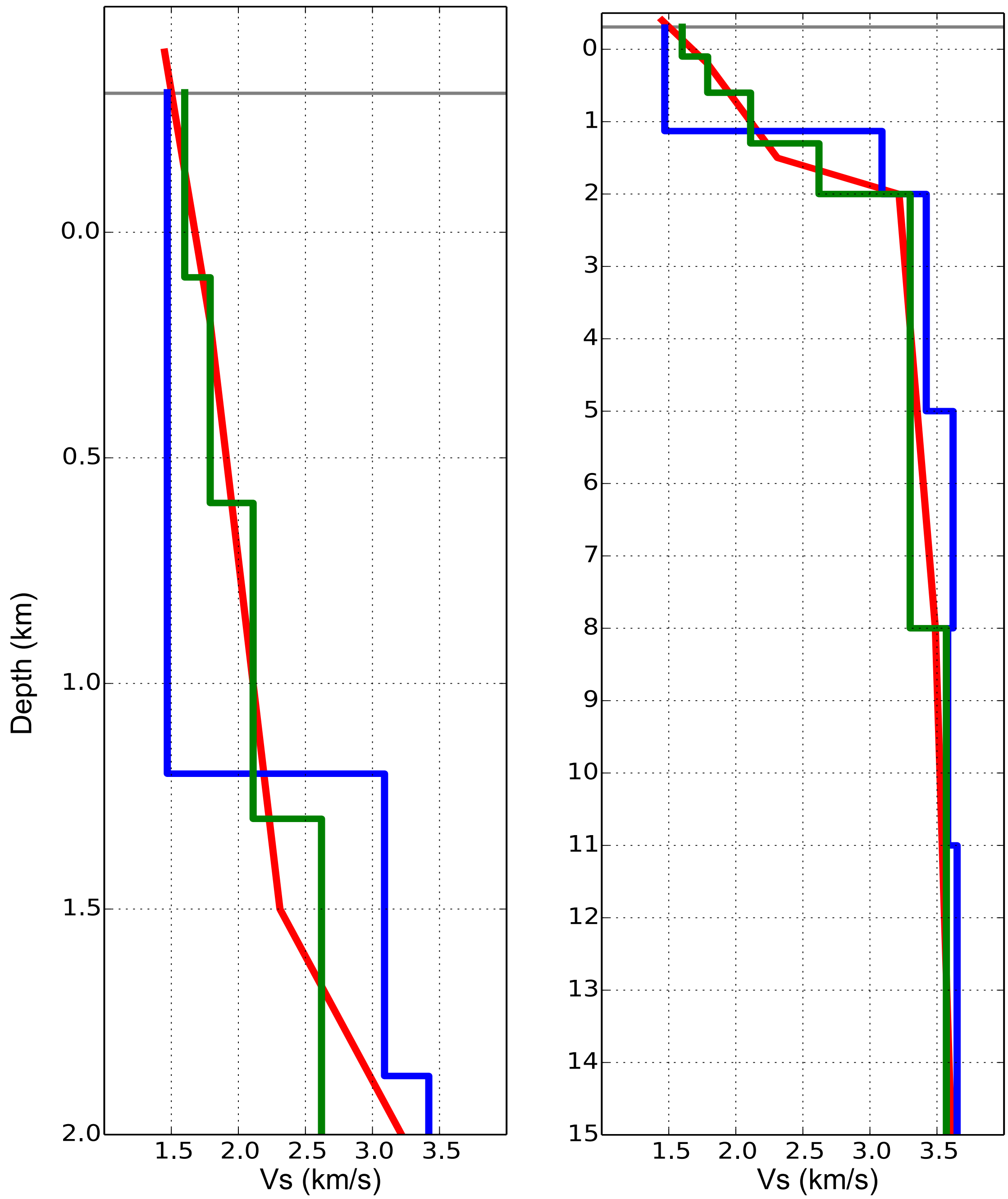

Figure 5: Left: Vs models from the Wilzetta Fault area down to 2km deep, the top of crystalline basement (Luza and Lawson, 1983). **Right:** Velocity models down to 15 km. *Blue*: final 1D model used in Keranen et al. (2013); *Red*: gradient-based starting model used in this study (input for NonLinLoc); *Green*; discrete-layer minimum 1D model generated with Velest and used in this study (input for FMTomo)

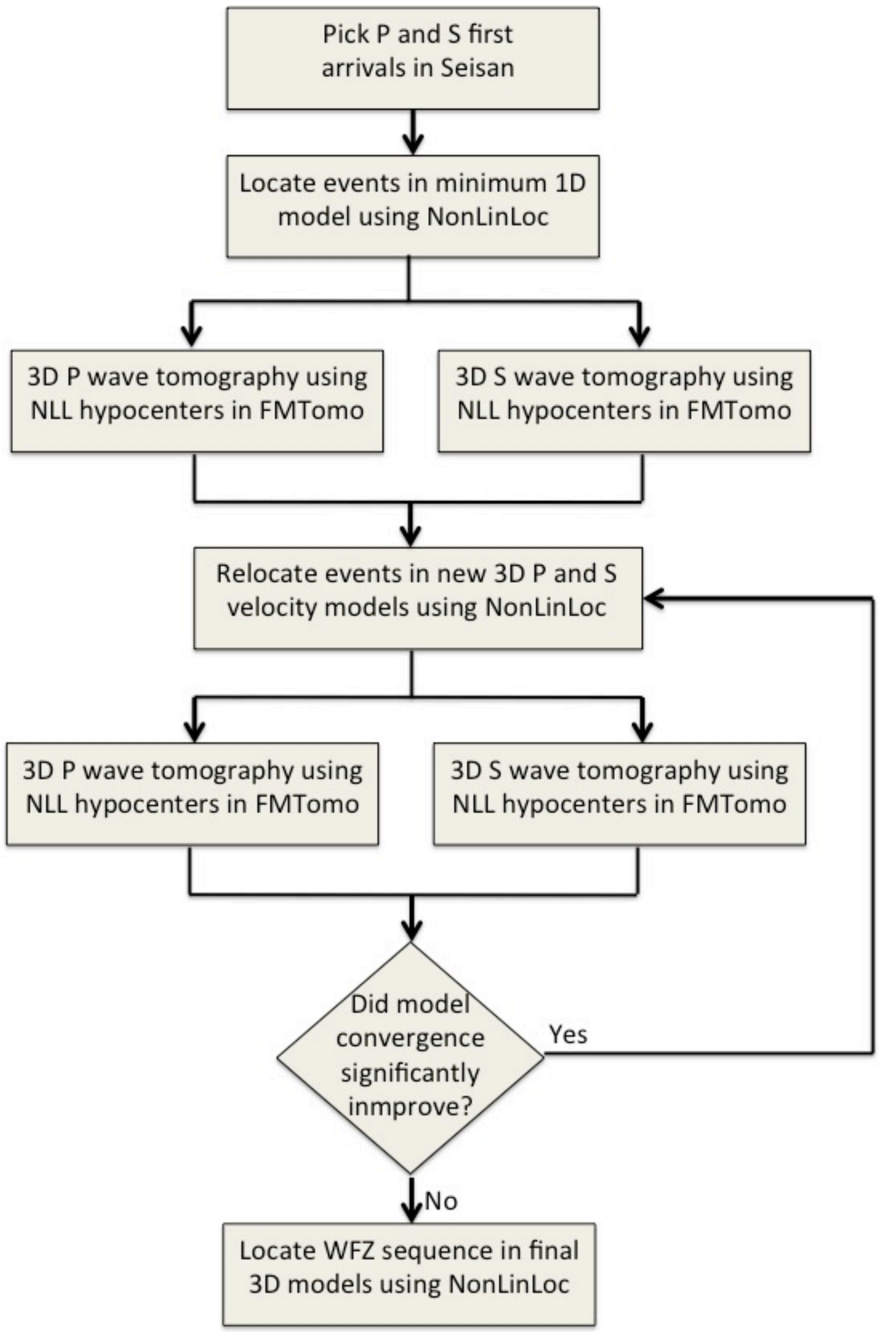

Figure 6: Flow-chart summarizing the processing steps used in this study. Three software packages were used in this study: Seisan to pick first arrivals, NonLinLoc to locate hypocenters in 1D and 3D velocity models, and FMTomo to perform 3D tomographic inversion.

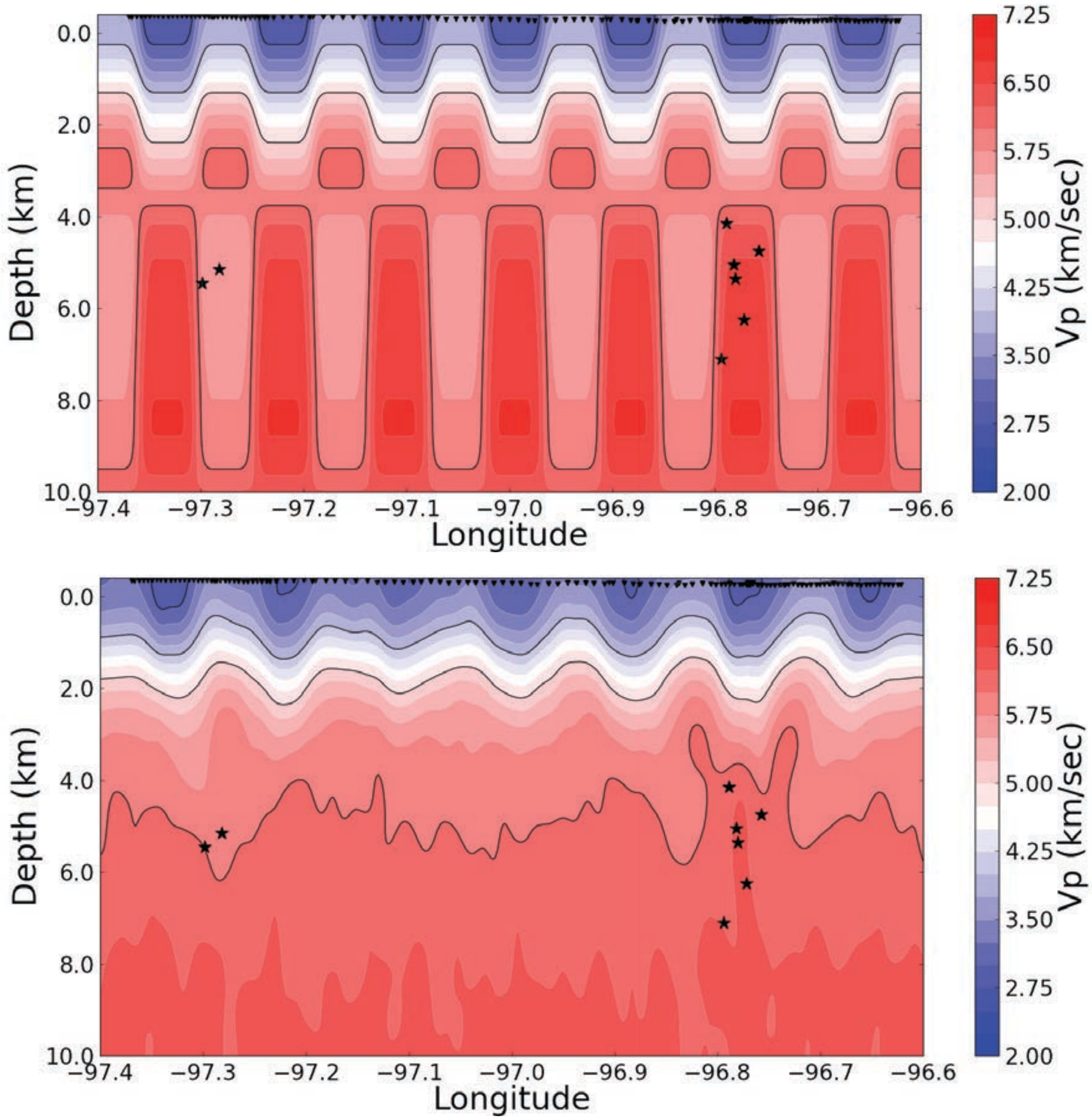

Figure 7: Top: Initial Vp checkerboard model with 5km x 5km x 5 km anomalies. **Bottom:** Recovered Vp anomaly distribution indicates that velocity features ~5km in length are resolvable throughout the model to ~4km depth. Inverted triangles indicate receiver locations; stars indicate source locations.

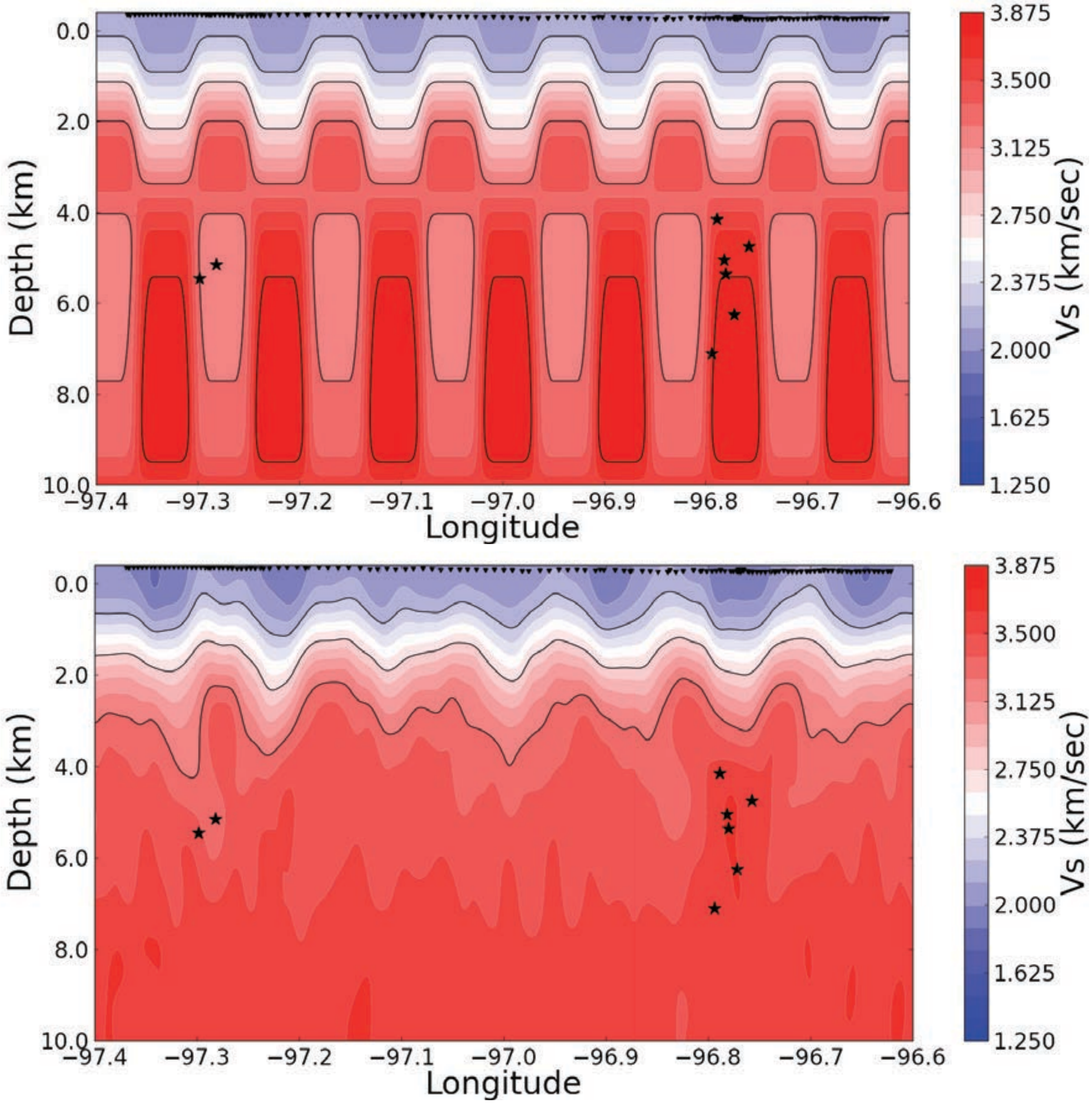

Figure 8: Top: Initial Vs checkerboard model with 5km x 5km x 5 km anomalies. **Bottom:** Recovered Vs anomaly distribution indicates that velocity features ~5km in length are resolvable through most of the top 4km of the study area.

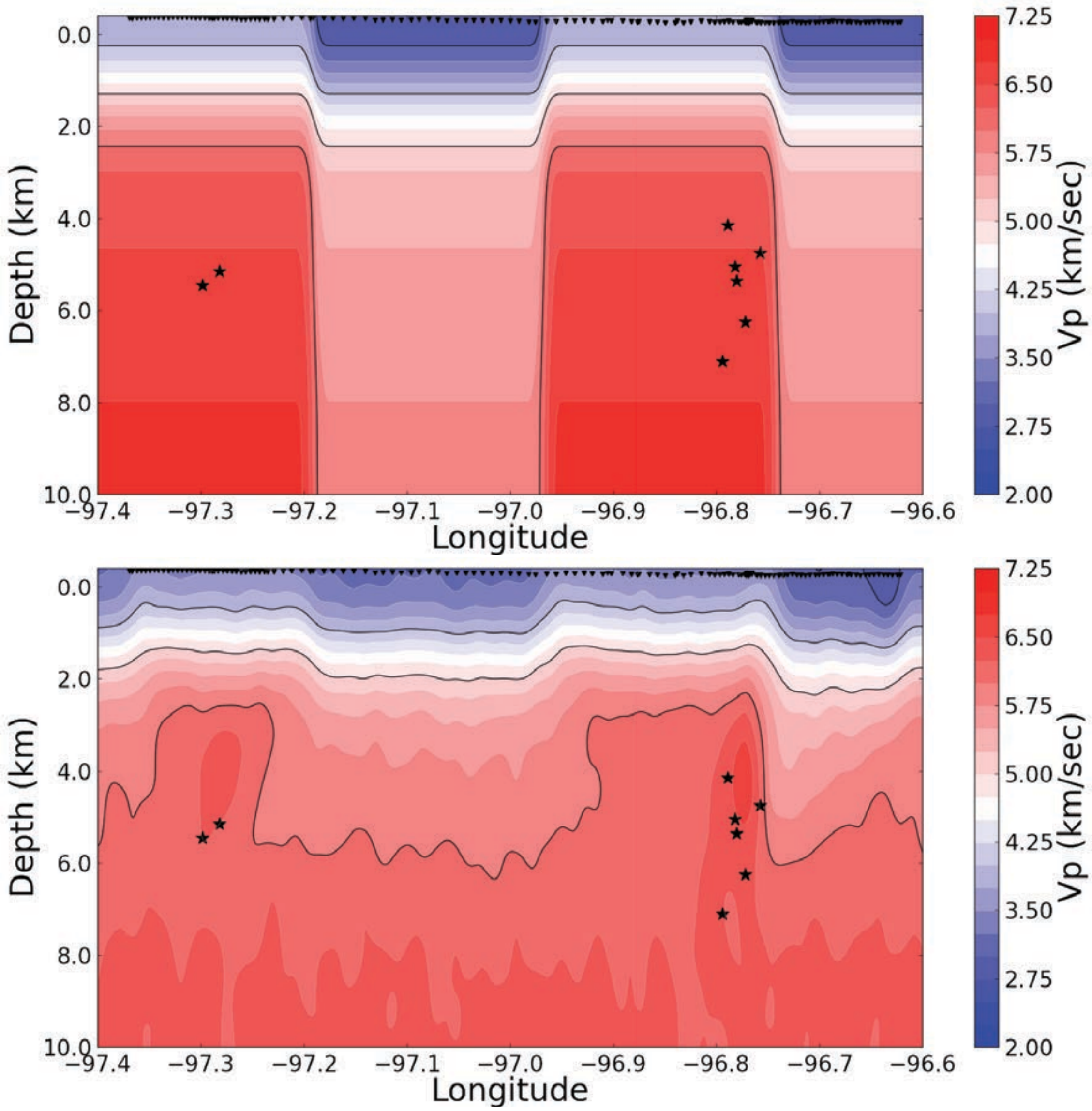

Figure 9: Top: Initial Vp checkerboard model with 20km x 20km x 20 km anomalies. **Bottom:** Recovered Vp anomaly distribution shows that broad wavelength features are resolvable between the source regions down to ~6 km.

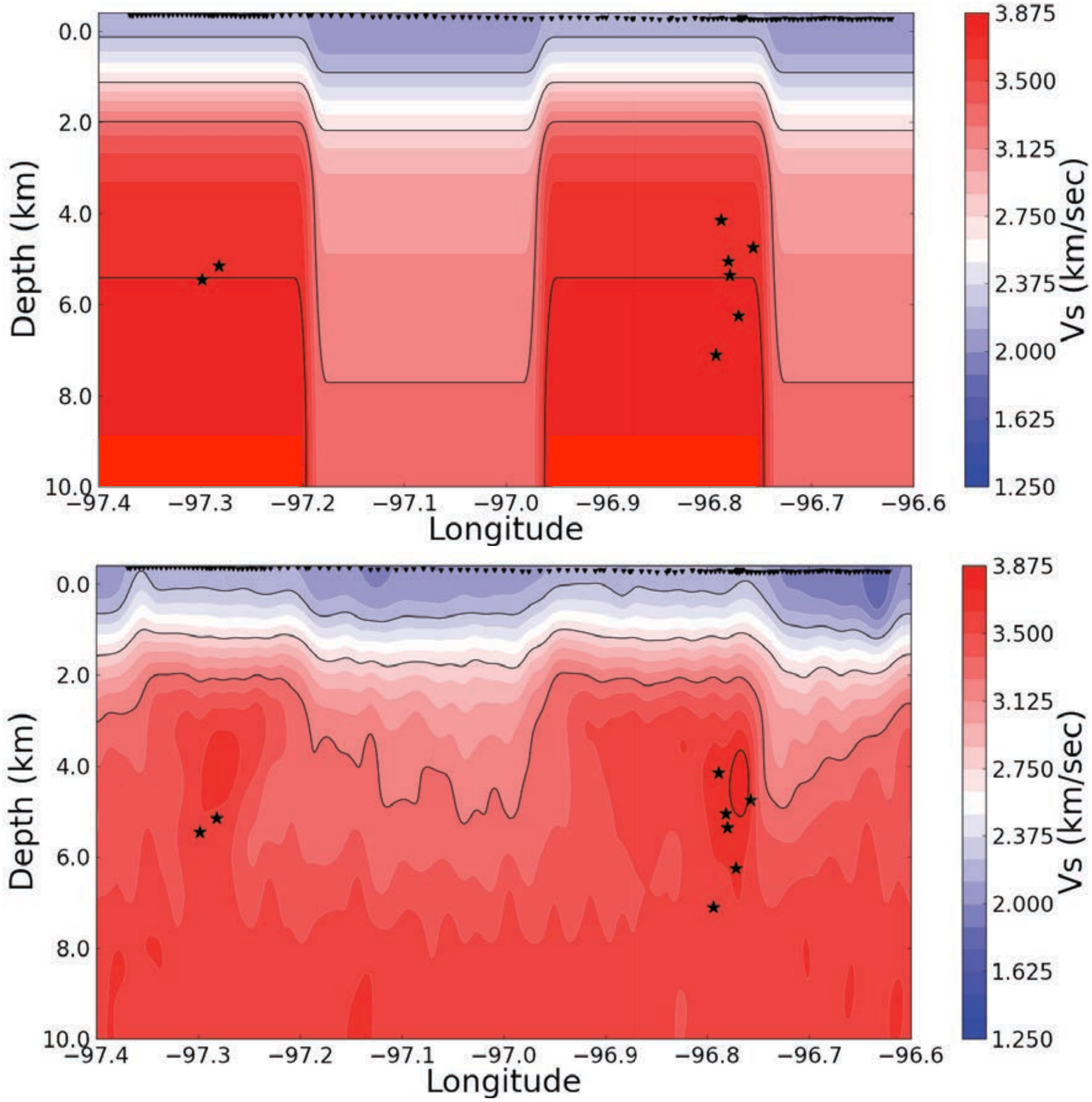

Figure 10: Top: Initial Vs checkerboard model with 20km x 20km x 20 km anomalies. **Bottom:** Recovered Vs anomaly distribution shows that broad wavelength features are resolvable between the source regions down to ~8 km.

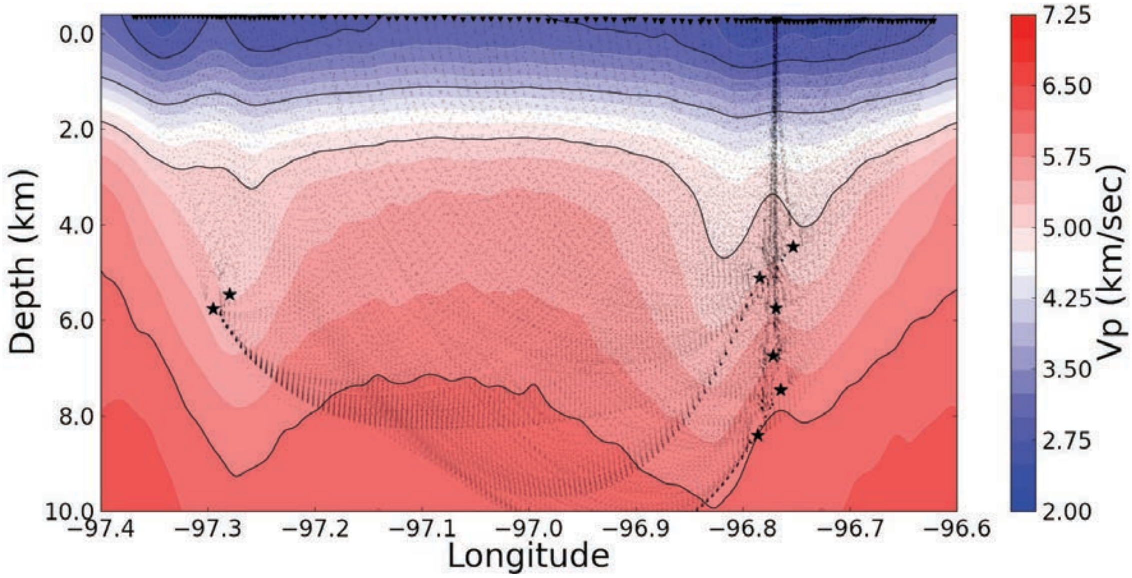

Figure 11: Tomographic Vp cross-section generated from hypocenters located in the minimum 1D velocity model. Model misfit is 111ms. Faded grey dots represent ray coverage.

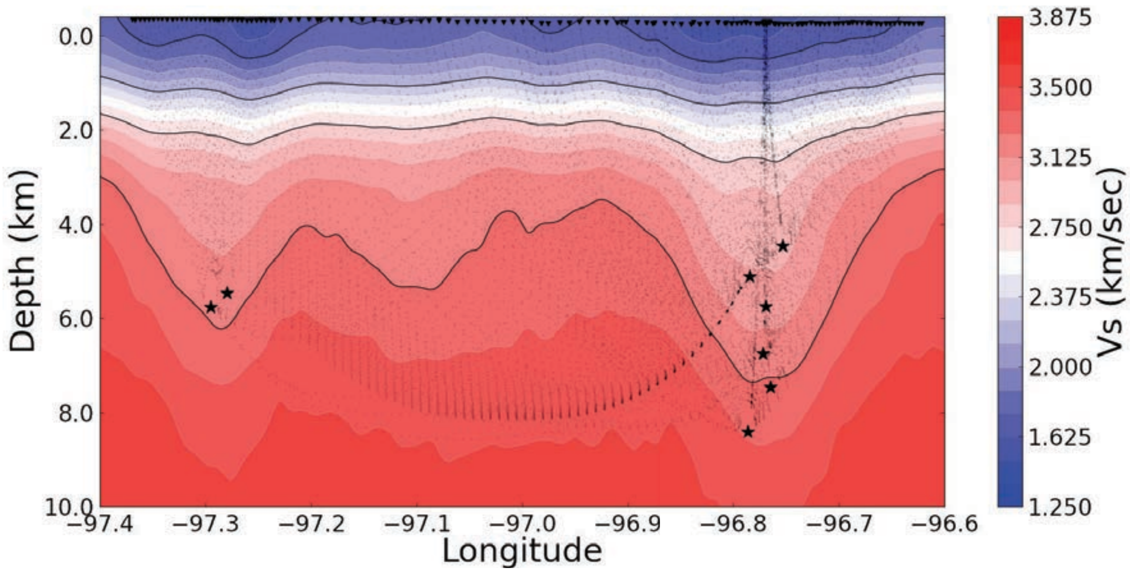

Figure 12: Tomographic Vs cross-section generated from hypocenters located in the minimum 1D velocity model. Model misfit is 162ms. Faded grey dots represent ray coverage.

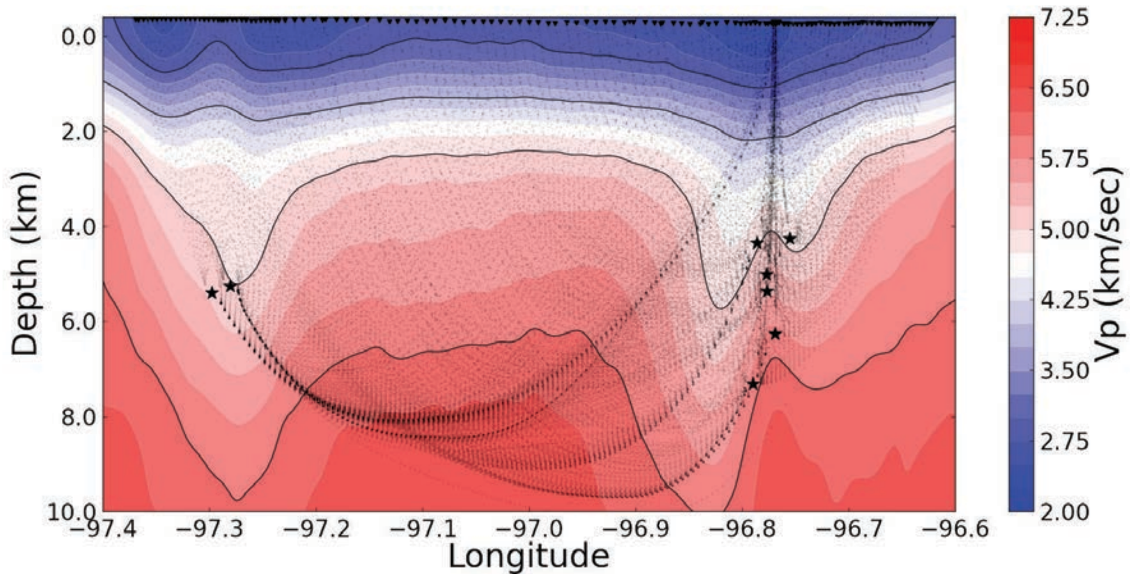

Figure 13: Refined tomographic Vp model using hypocenters located in the velocity model shown in Fig. 9, and using that velocity model as the starting model for a second FMT iteration. Final model misfit is 92ms.

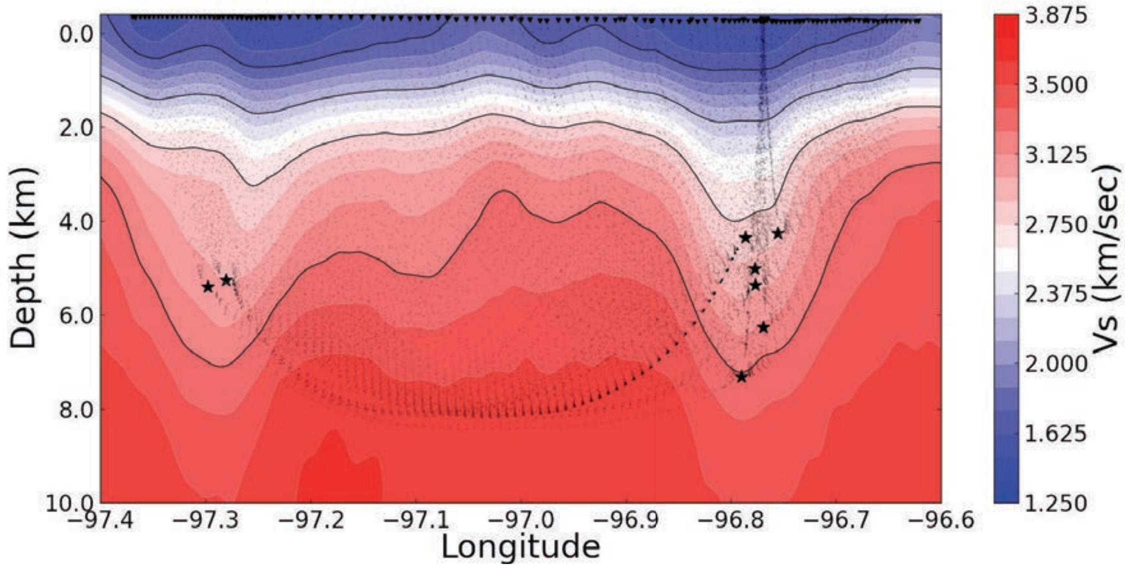

Figure 14: Refined tomographic Vs model using hypocenters located in the velocity model shown in Fig. 10, and using that velocity model as the starting model for a second FMT iteration. Final model misfit is 142ms.

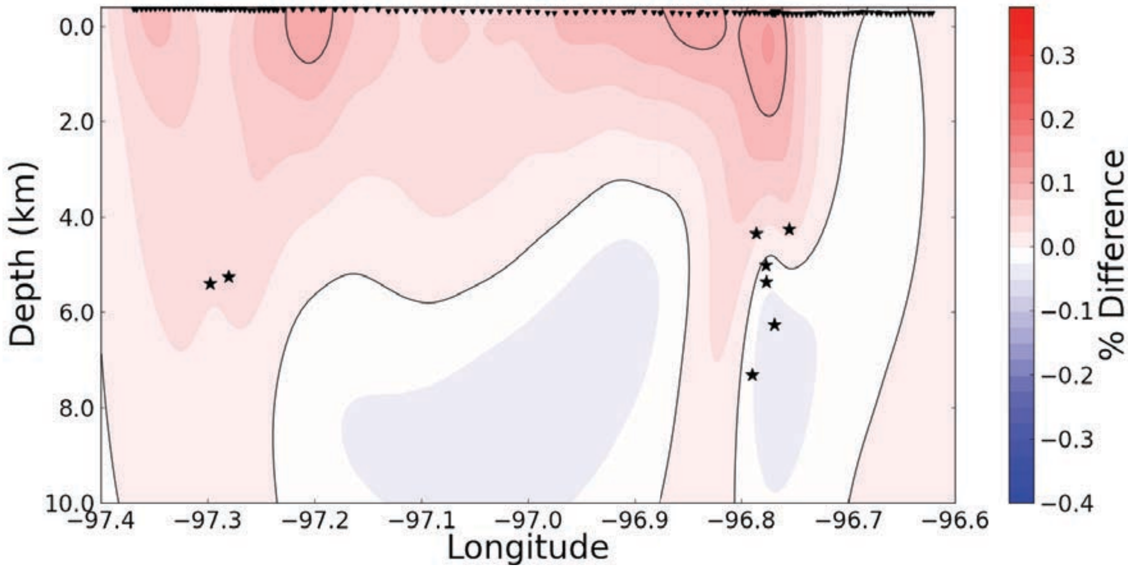

Figure 15: Cross-section showing the percent difference in Vp between the inversion using hypocenters located in a 1D model (Fig. 9) and the refined model using hypocenters relocated in the 3D tomographic model (Fig. 11). Blue areas are where the refined model is faster, and red indicates areas where the refined model is slower.

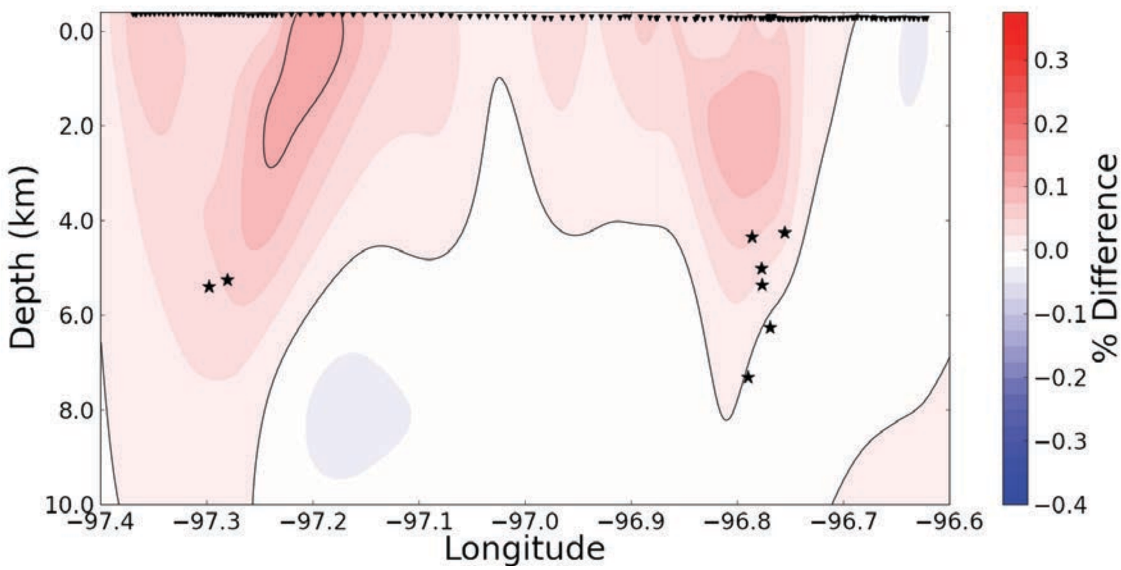

Figure 16: Cross-section showing the percent difference in Vs between the inversion using hypocenters located in a 1D model (Fig. 9), and the refined model using hypocenters relocated in the 3D tomographic model (Fig. 11). Blue areas are where the refined model is faster, and red indicates areas where the refined model is slower.

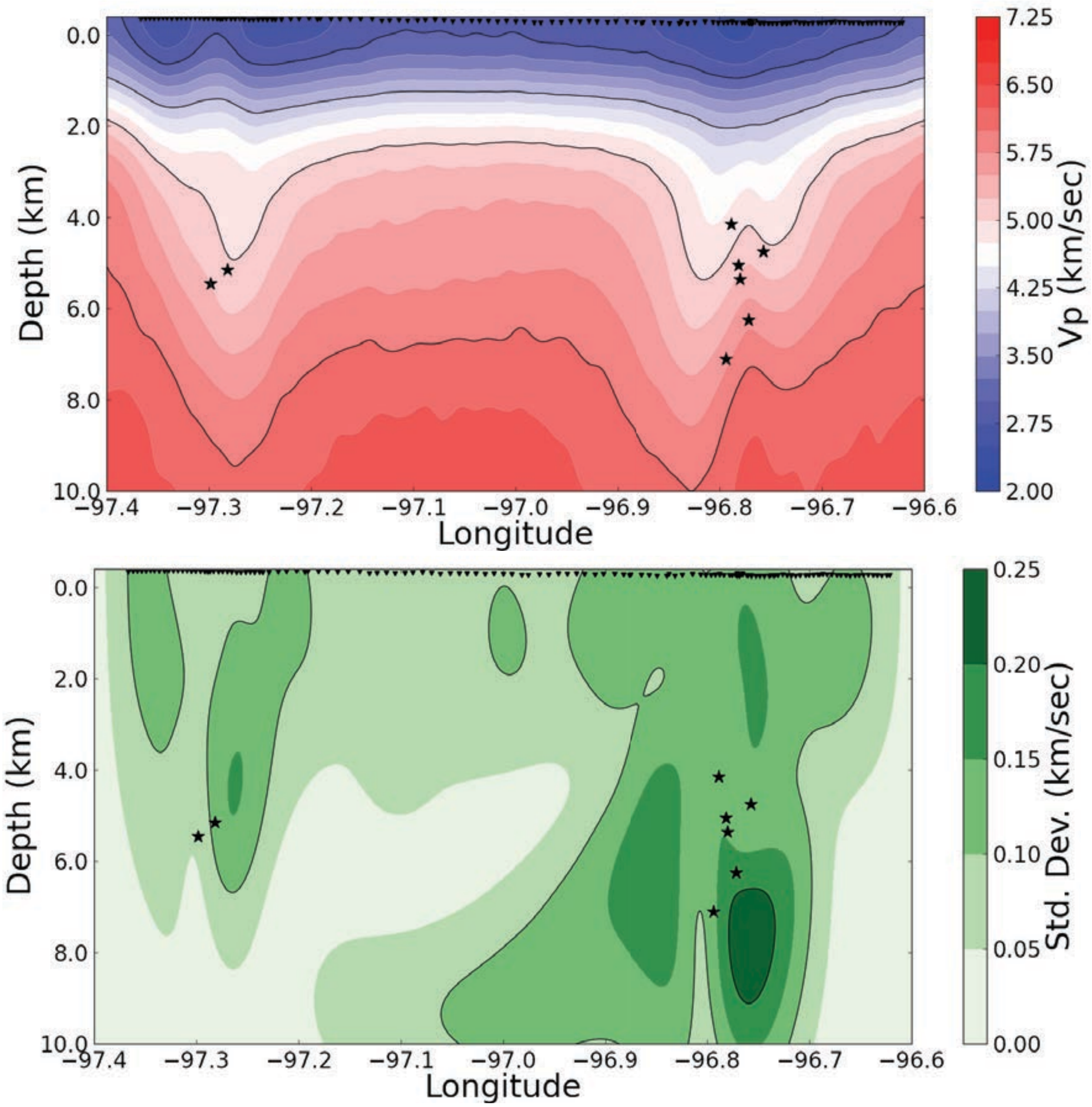

Figure 17: Top: Cross-section of average Vp model of the jackknifed inversions, showing a high degree of similarity to the inversion of all 8 earthquakes (Fig. 13). **Bottom:** Cross-section of the Vp standard deviation of the jackknifed inversions. Vp standard deviation rarely exceeds 0.2 km/sec, indicating a well-constrained velocity model.

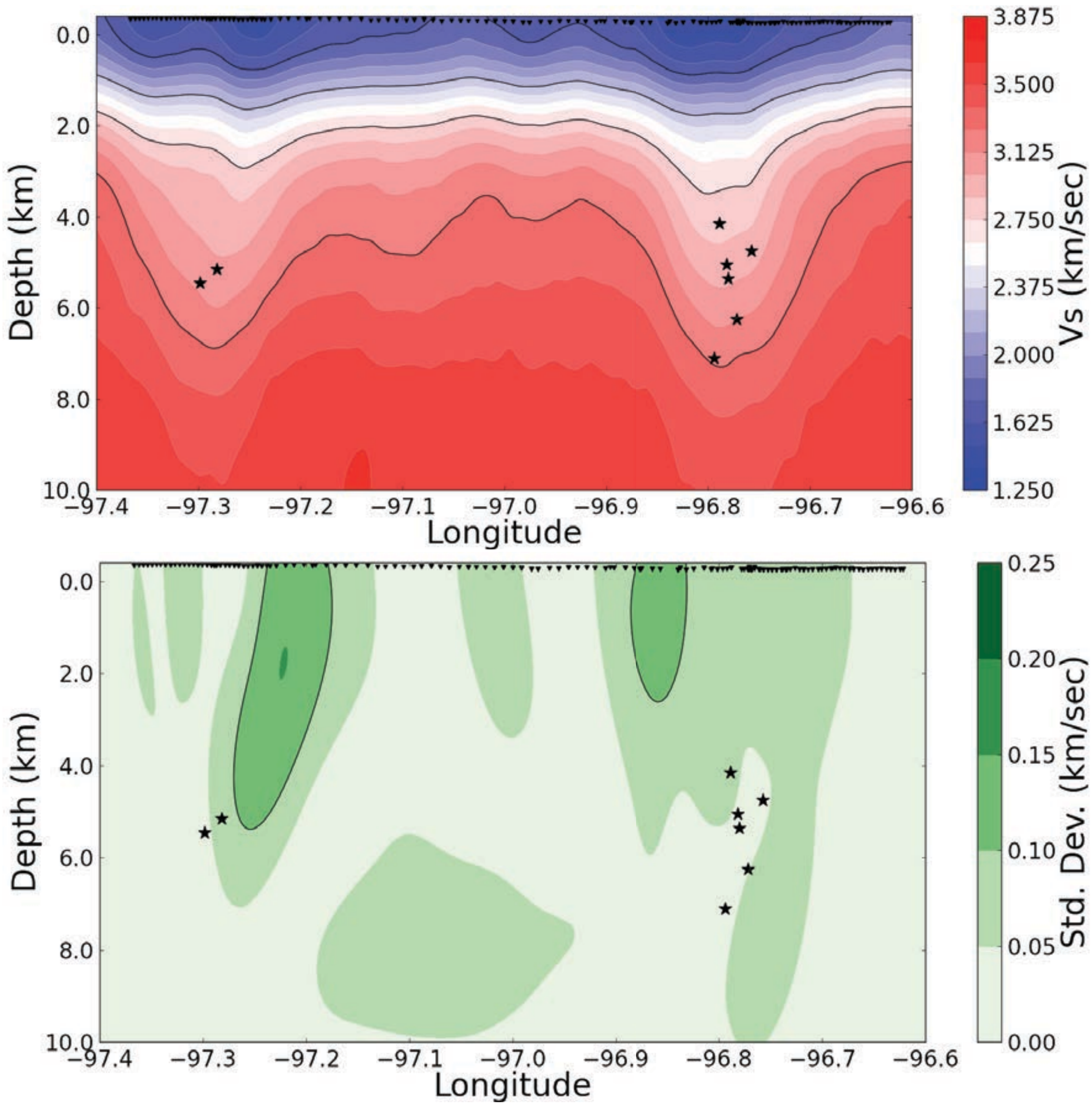

Figure 18: Top: Cross-section of average Vs model of the jackknifed inversions, showing a high degree of similarity to the inversion using all 8 earthquakes (Fig. 14). **Bottom:** Cross-section of the Vs standard deviation of the jackknifed inversions. Vs standard deviation rarely exceeds 0.15km/sec, indicating a well-constrained velocity model.

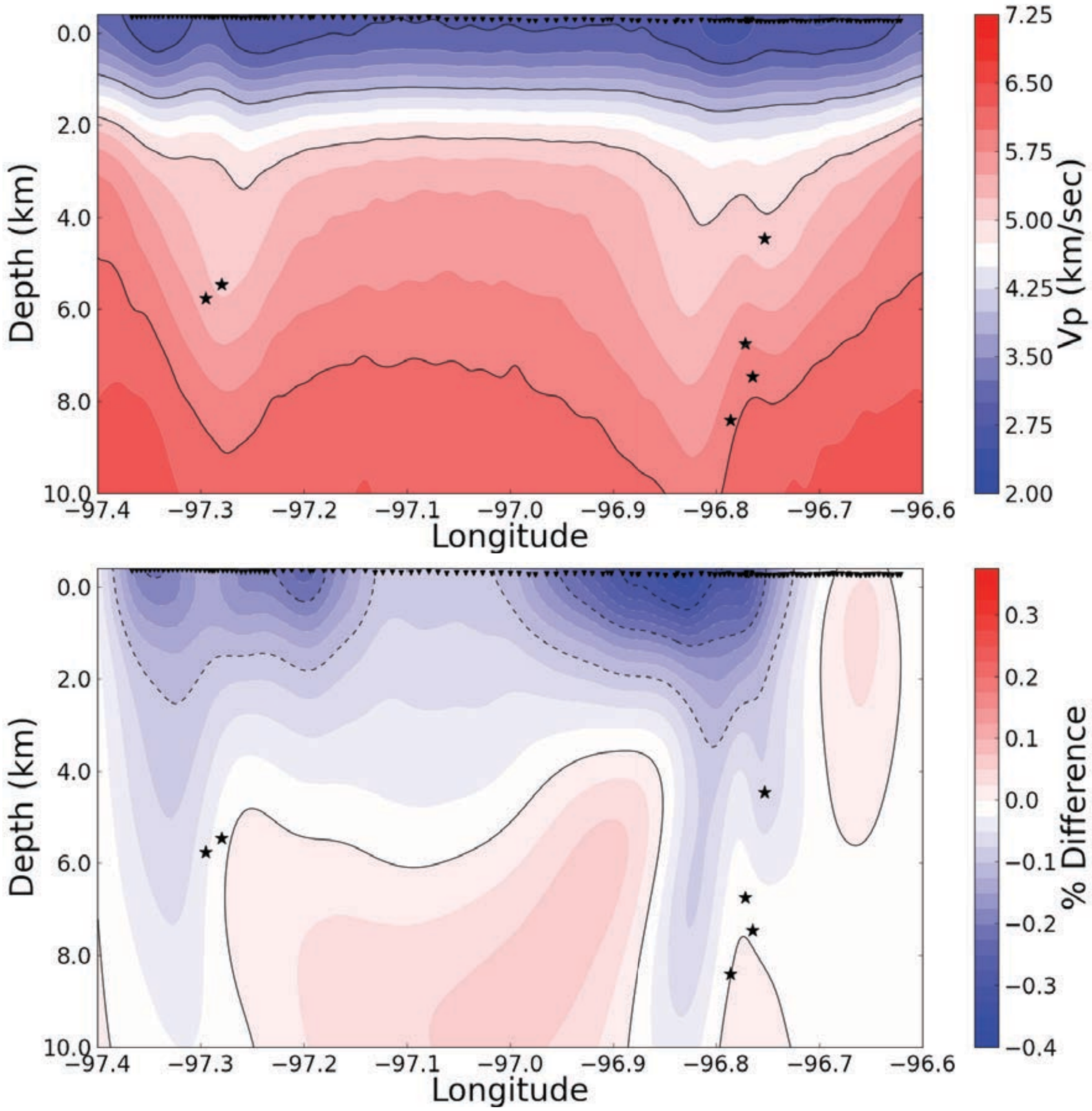

Figure 19: Top: Final Vp model generated from the jackknife dataset with the highest MAPD. **Bottom:** Cross-section showing the percent difference in Vp between the jackknifed model and the reference model using the whole dataset shown in figure 9. Blue areas are where the reference model is slower, and red indicates areas where the reference model is faster.

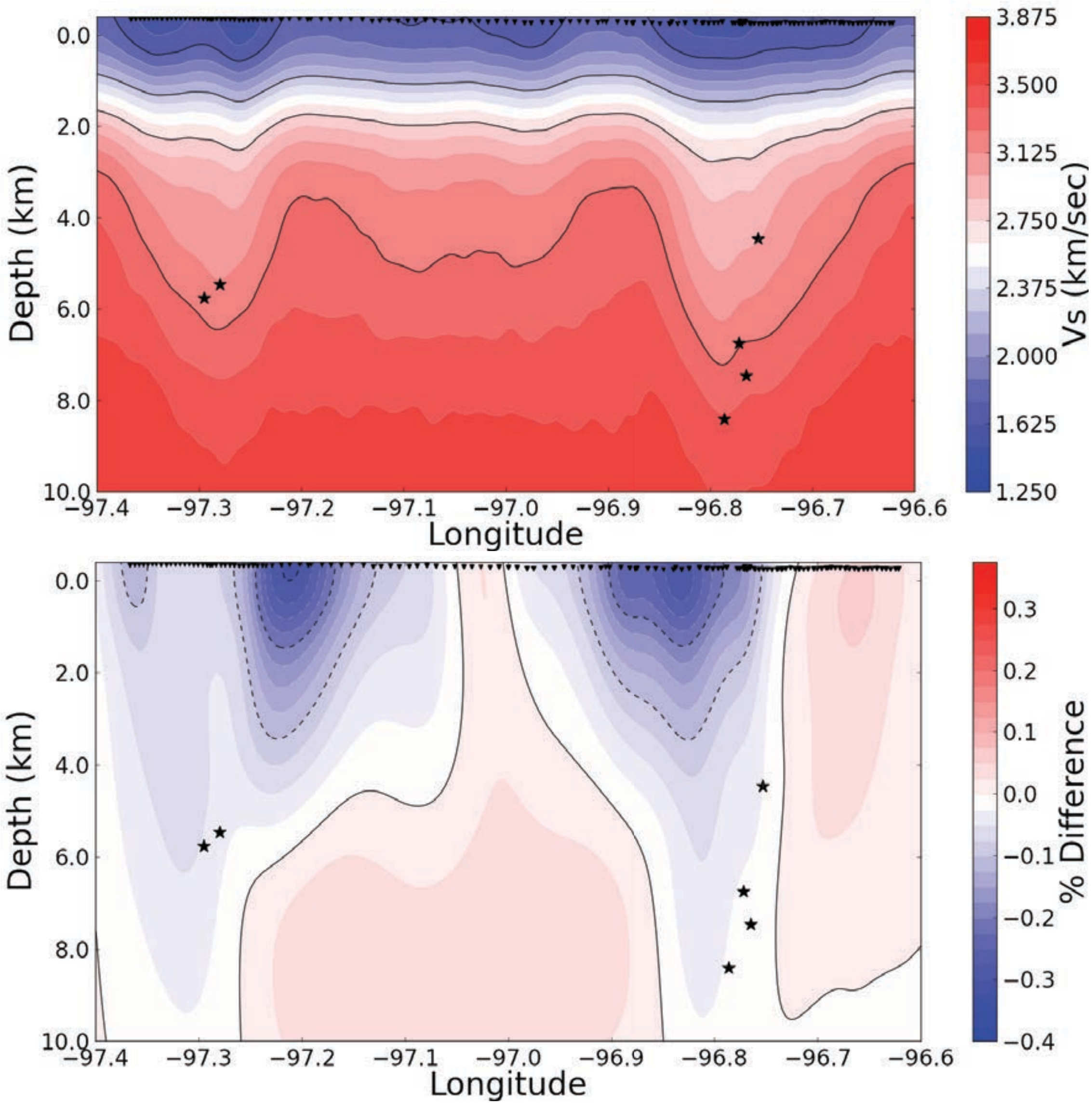

Figure 20: Top: Final Vs model generated from the jackknife dataset with the highest MAPD. **Bottom:** Cross-section showing the percent difference in Vs between the jackknifed model and the reference model using the whole dataset shown in Figure 9. Blue areas are where the reference model is slower, and red indicates areas where the reference model is faster.

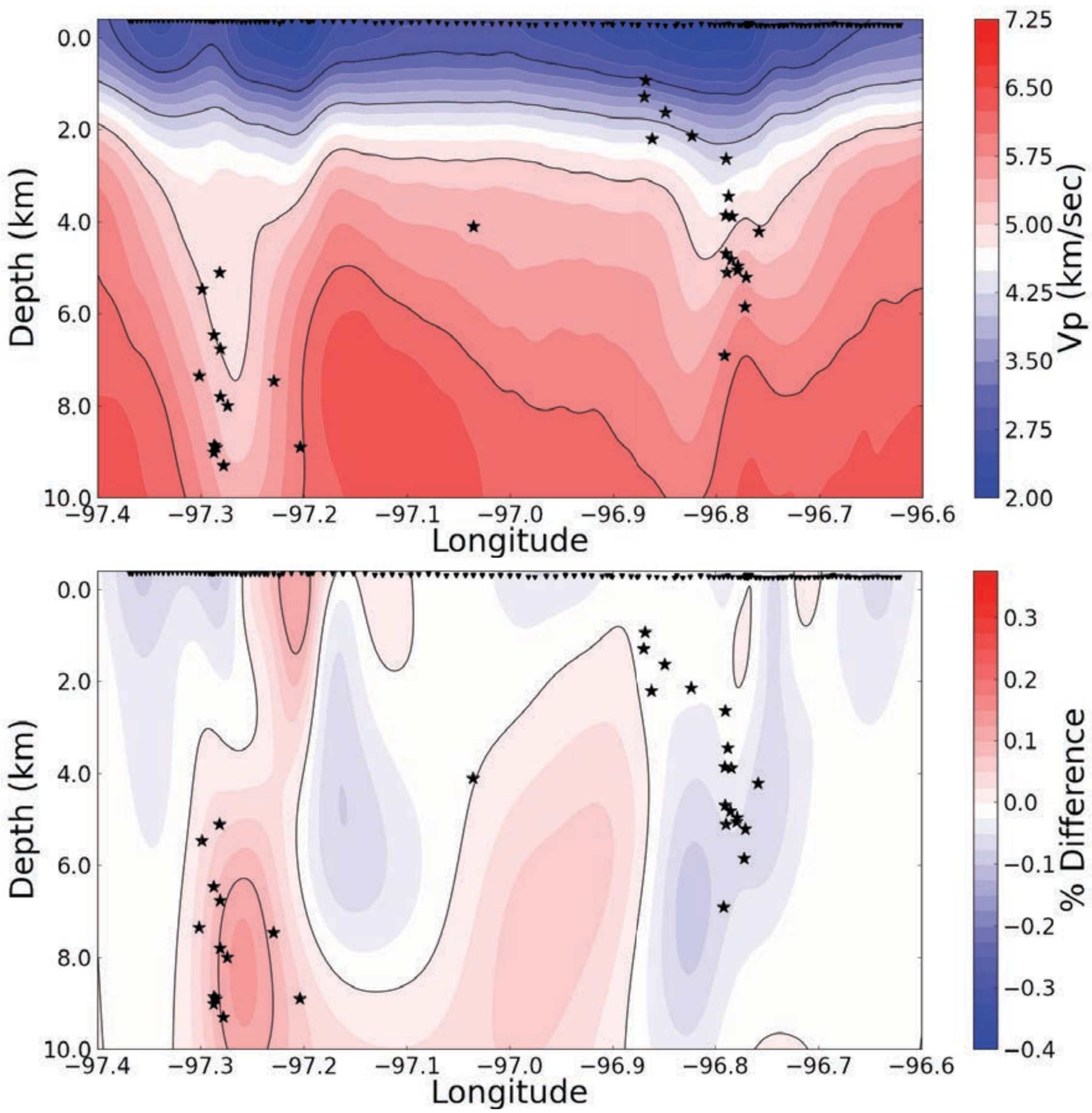

Figure 21: Top: Final inversion Vp model after 3D relocations of the augmented dataset. **Bottom:** Cross-section showing the difference in Vp between the augmented model and the reference model using shown in Figure 9. Blue areas are where the reference model is slower, and red indicates areas where the reference model is faster.

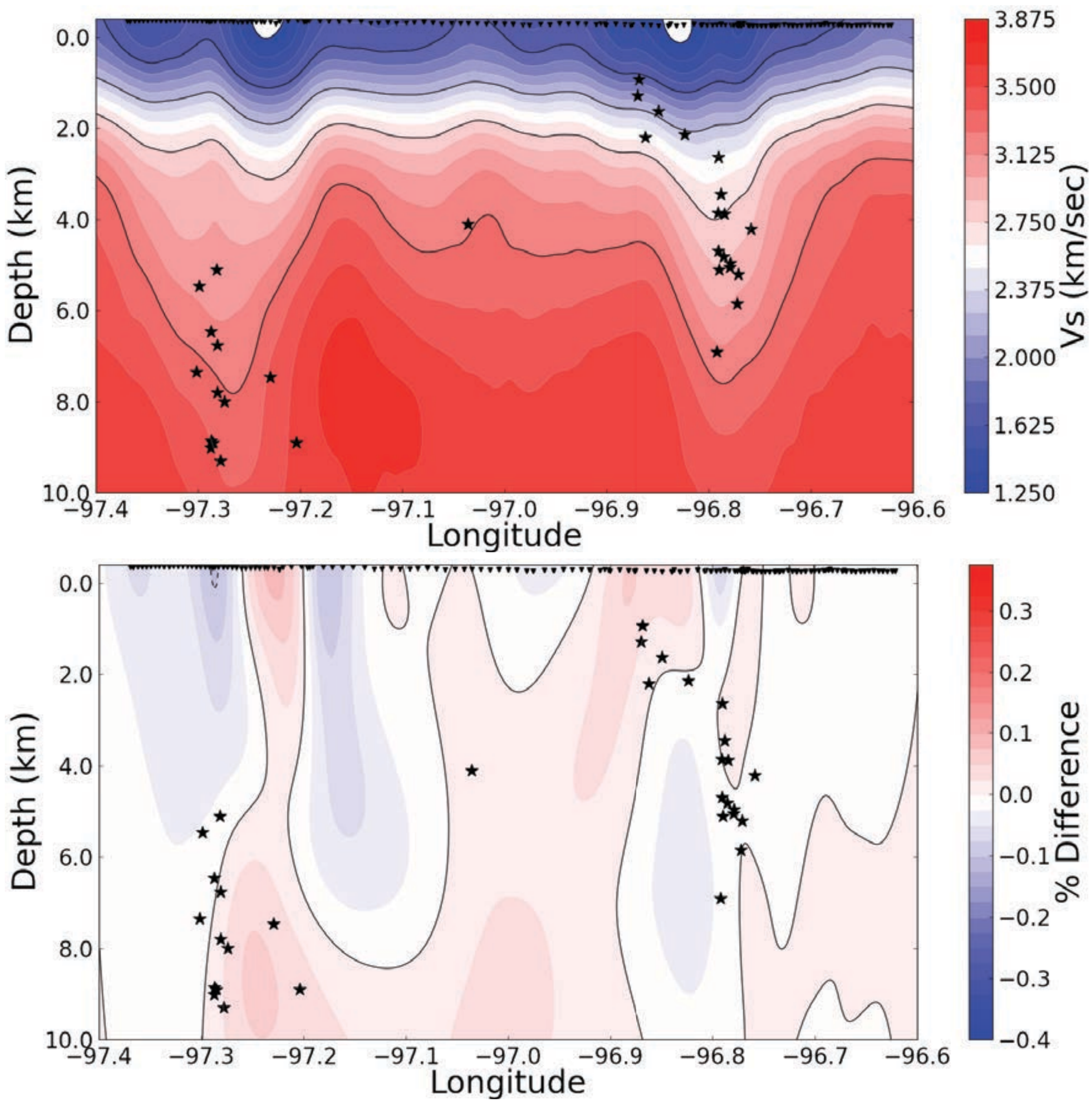

Figure 22: Top: Final inversion Vs model after 3D relocations of the augmented dataset. **Bottom:** Cross-section showing the difference in Vs between the augmented model and the reference model shown in Figure 9. Blue areas are where the reference model is slower, and red indicates areas where the reference model is faster.

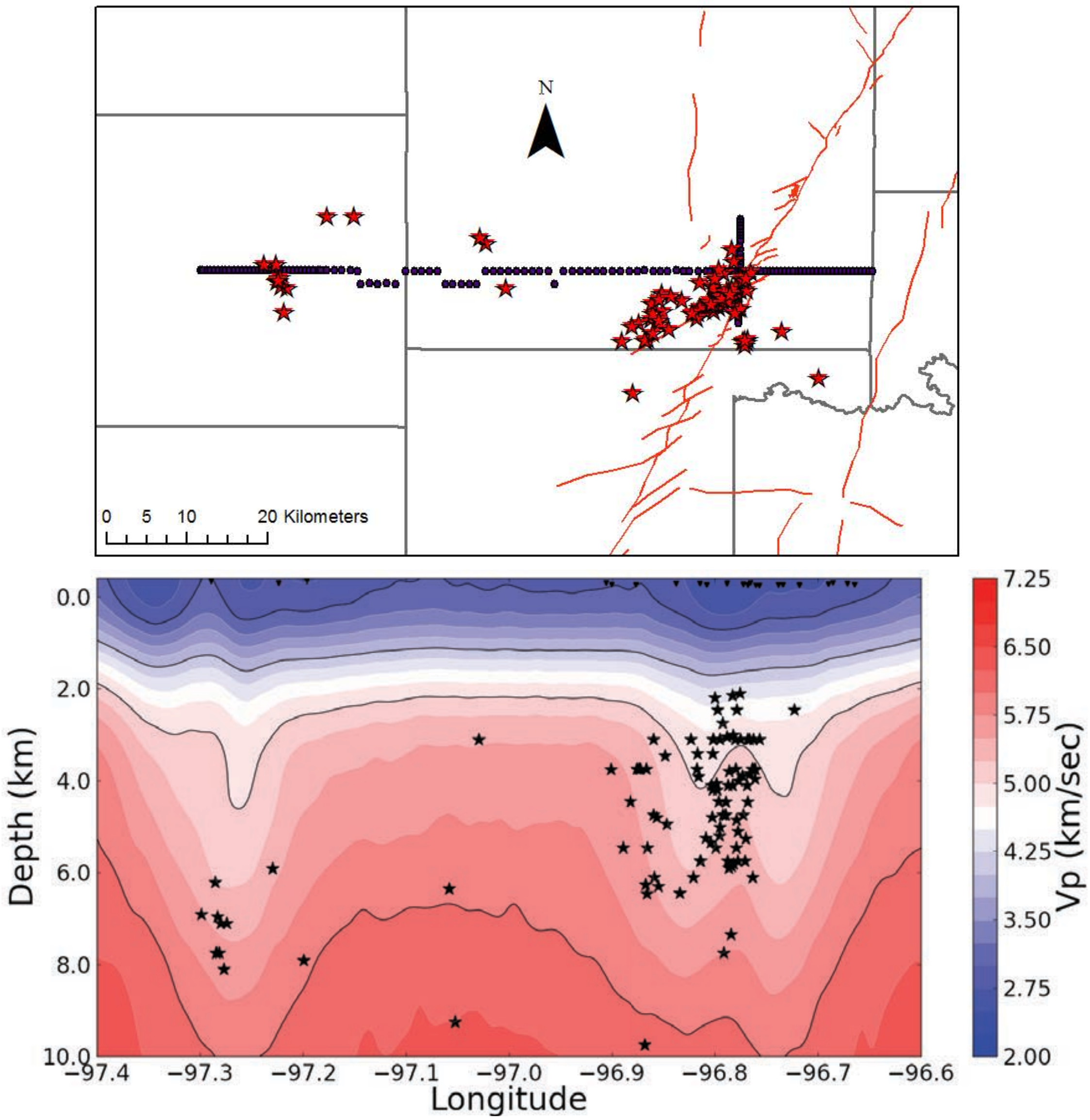

Figure 23: Top: Map-view of the hypocenters (red stars) relocated in the final 3D Vp tomographic model of Figure 9. The Meeker-Prague Fault delineates a southeast boundary for most of the WFZ seismicity, suggesting a northwesterly dip. **Bottom:** Cross-section showing the depths and positional relation of hypocenters to velocity anomalies. None of the hypocenters were located above 2.0km below MSL, which is interpreted to be the top of basement in the area.

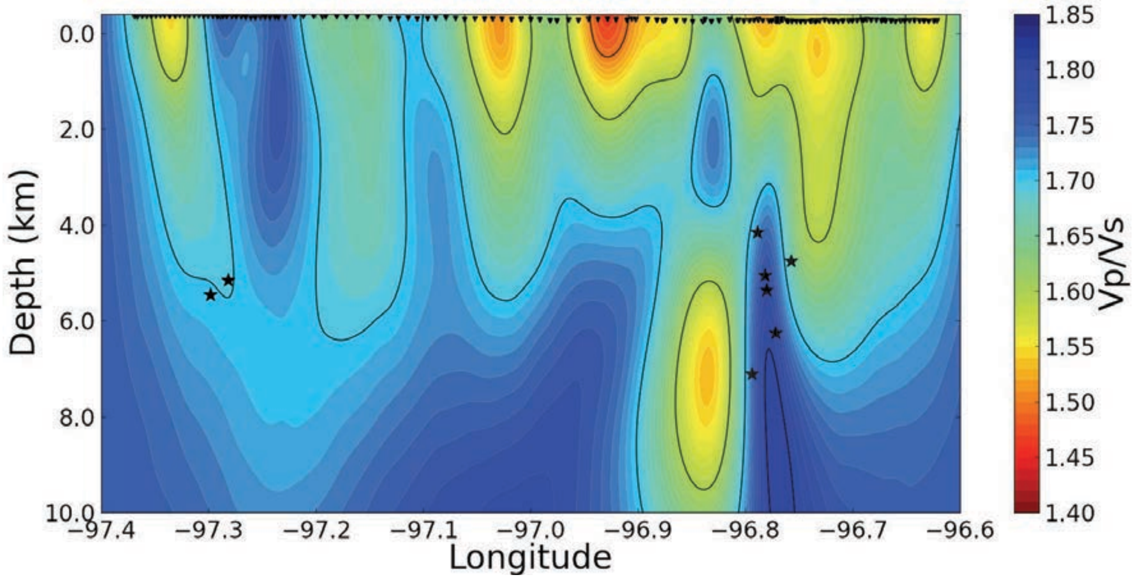

Figure 24: Latitudinal cross-section showing the Vp/Vs ratio of the model. A general low Vp/Vs ratio is apparent, but since the resolution of the Vp/Vs model is uncertain, individual anomalies seen here may not be physically meaningful.

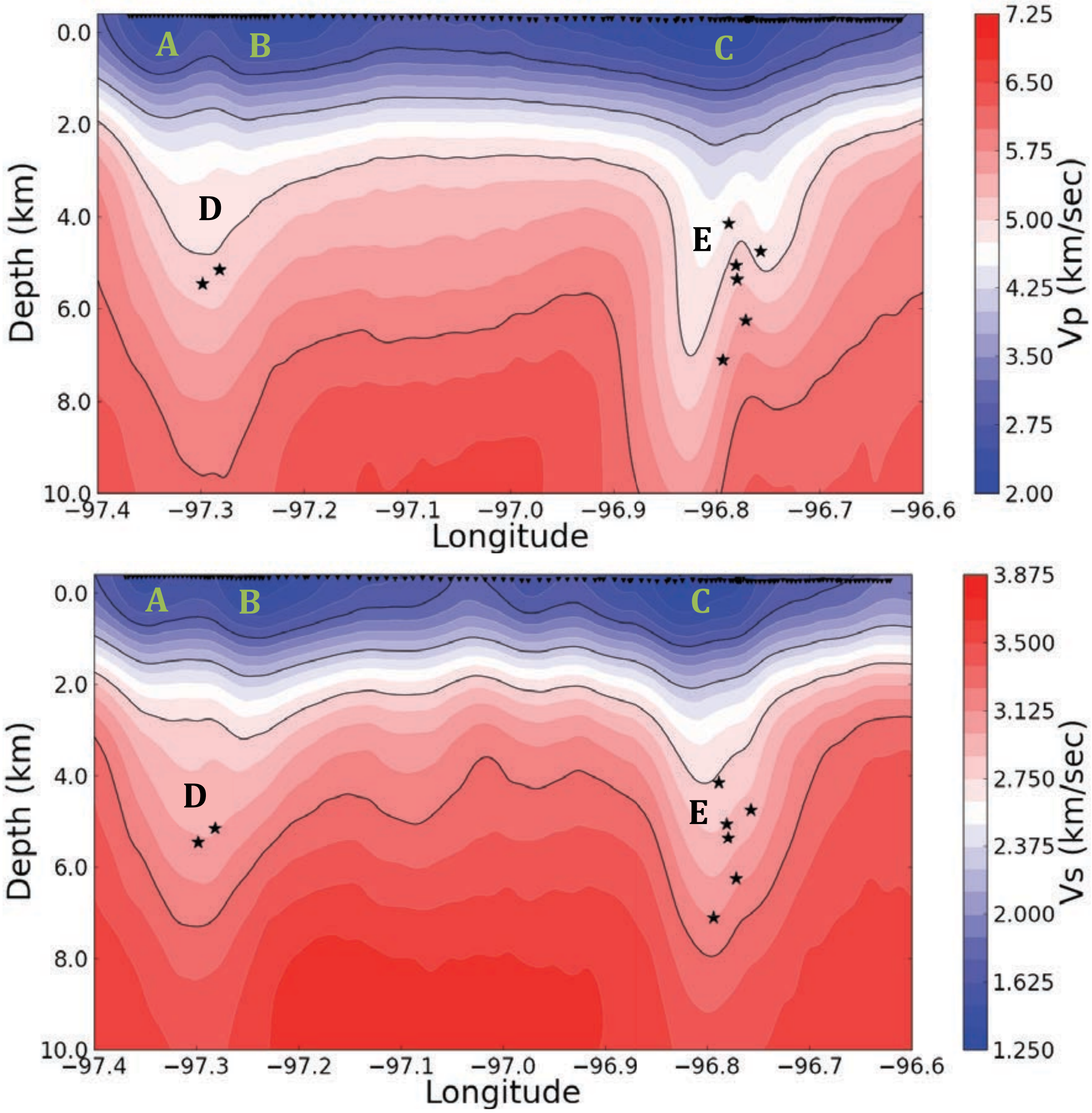

Figure 25: Top: Annotated cross-section of final Vp model (Fig. 9). **Bottom:** Annotated cross-section of final Vs model (Fig. 10). Anomalies A and B correlate with locations the Canadian River transects the E-W instrument line, anomaly C and E correlate with the WFZ, and anomaly D correlates with the Jones source region.

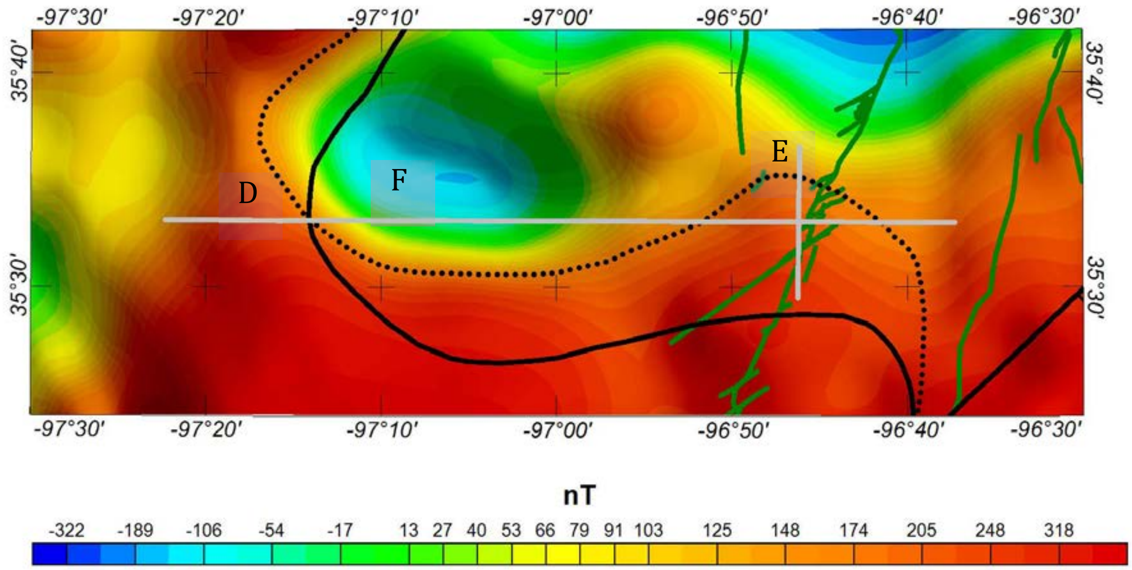

Figure 26: Reduction-to-pole map of the magnetic field intensity in the area. Grey lines show the locations of receiver lines; Green lines indicate faults mapped by (Dycus, 2013); Solid black line represents the basement lithology contacts (Denison, 1981); Dotted black lines represent a modified basement contact interpreted from the velocity models and RTP map. Anomalies D and E in the tomography correlate with positive magnetic anomalies, and a strong negative anomaly, F, are observed adjacent to the E-W instrument line.

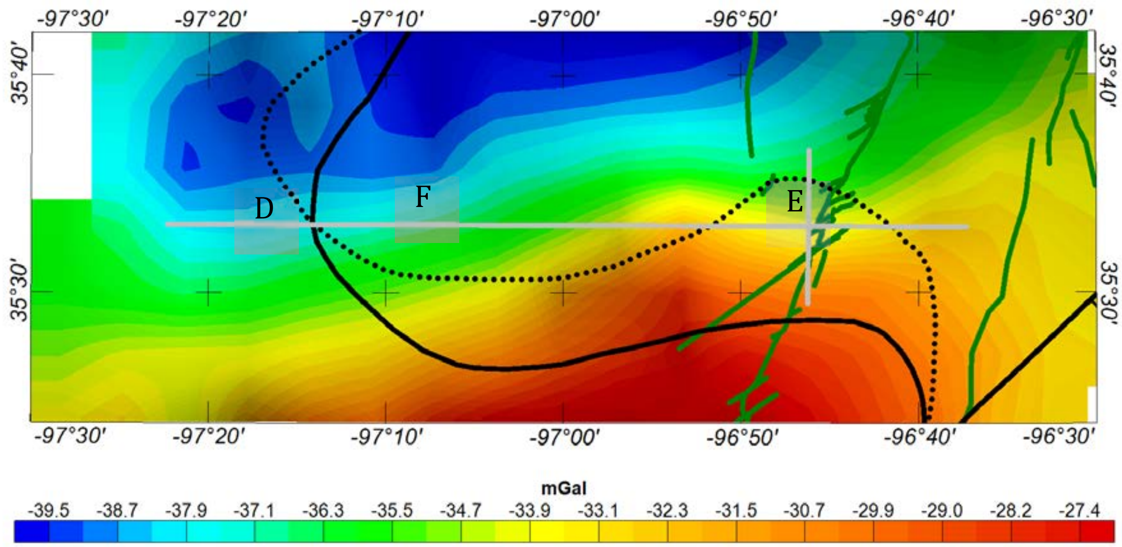

Figure 27: Residual of a 5km upward continuation on the complete Bouguer anomaly map for the study area. Grey lines show the locations of receiver lines; Green lines indicate faults mapped by (Dycus, 2013); Solid black line represents the basement lithology contacts (Denison, 1981); Dotted black lines represent a modified basement contact interpreted from the velocity models and RTP map. Anomaly D does not correlate to any observed gravity feature, but anomaly E correlates to a weak negative gravity anomaly, and anomaly F correlates with a strong negative gravity anomaly.

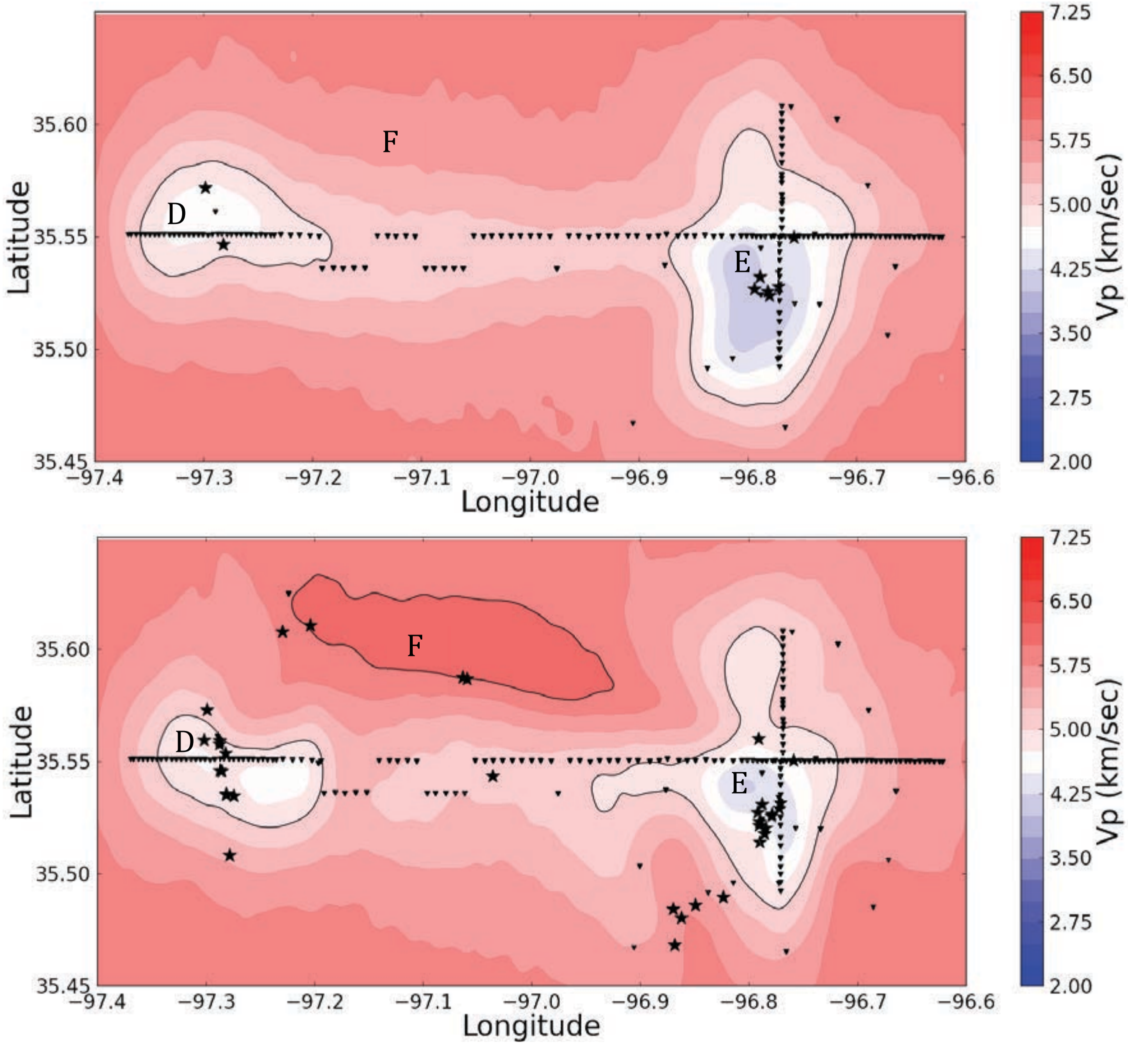

Figure 28: Top: 3km depth slice of final Vp model from the inversion using the 8 well-constrained earthquakes. **Bottom:** 3km depth slice of the Vp model generated from the augmented dataset. By including additional data, anomaly F, which is present on the potential field maps, starts being resolved in the tomography.

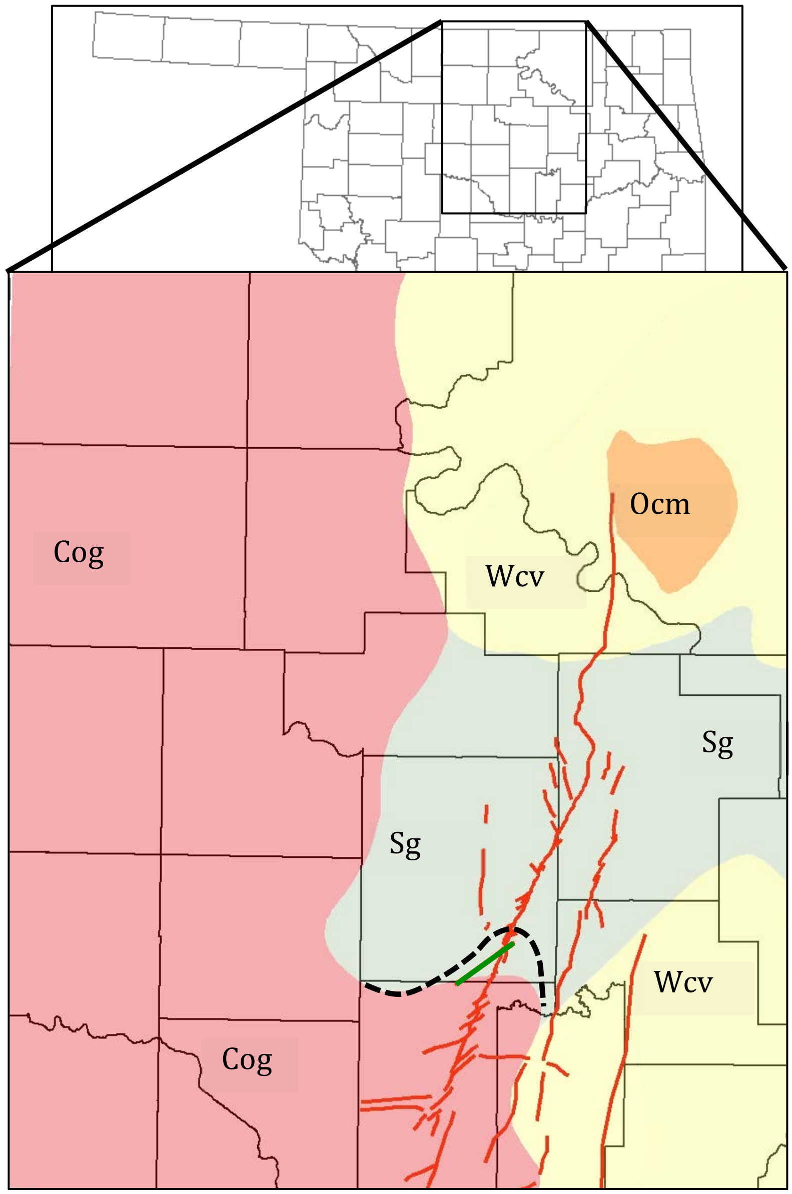

Figure 29: Basement lithology map of north-central Oklahoma, modified from Luza and Lawson (1983). Red lines are faults mapped by Dycus (2013); Green line represents the Meeker-Prague Fault; dashed black line represents a modified basement contact interpreted from the velocity models and RTP map, which is locally subparallel to the Meeker-Prague Fault; Sg: Spavinaw Granite Group; Wcv: Washington County Volcanic Group; Ocm: Osage County Microgranite; Cog: Central Oklahoma Granite Group.

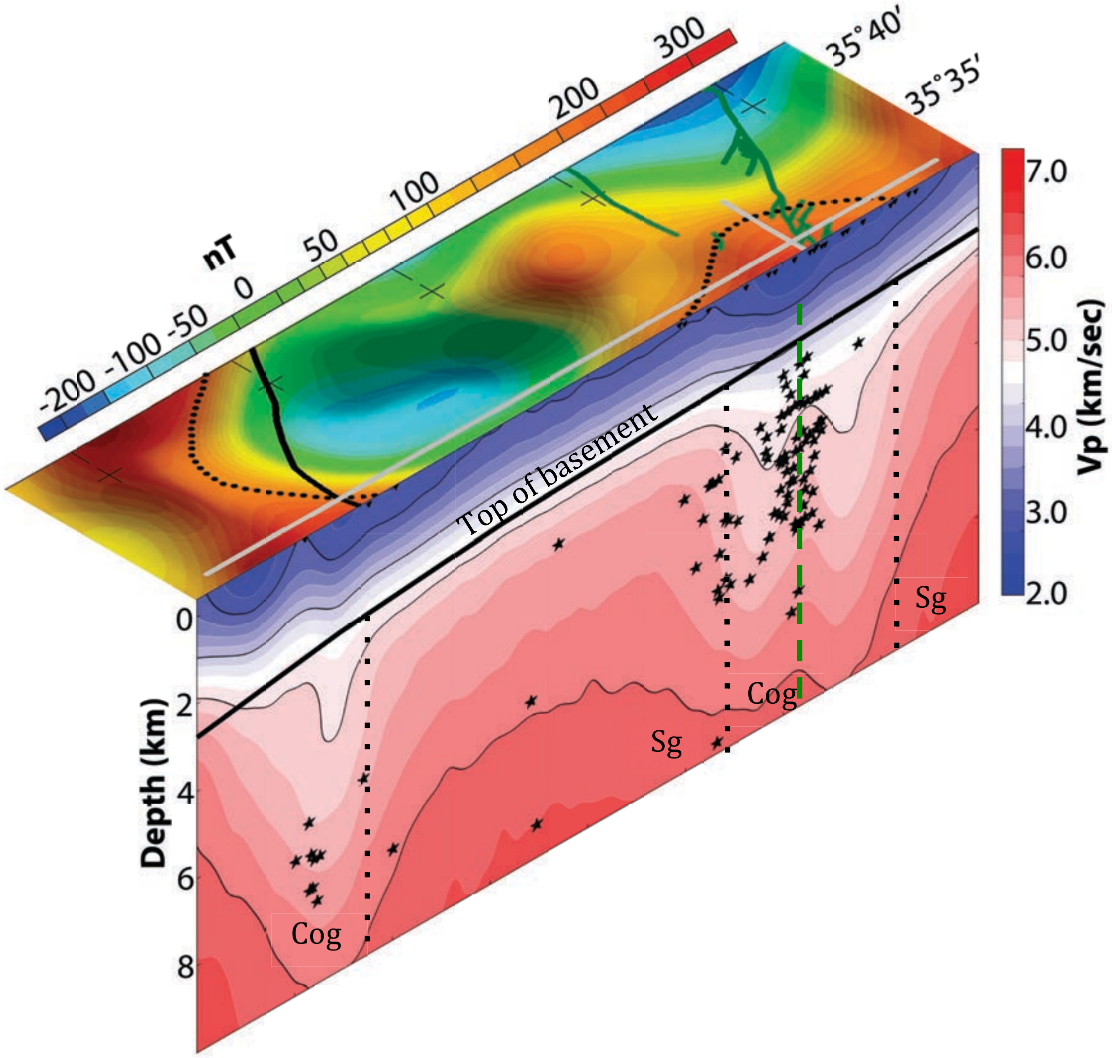

Figure 30: Block diagram illustrating the relationship between features seen in the tomography and features seen in the RTP magnetic map. Dotted black line represents modified basement lithology contacts; Dashed green line represents WFZ projected into the basement; Cog: Central Oklahoma Granite Group; Sg: Spavinaw Granite Group. Changes in basement velocities correlate strongly with strong magnetic anomalies, suggesting a change in basement lithology.

References

Brocher, T. M., 2008, Compressional and Shear-Wave Velocity versus Depth Relations for Common Rock Types in Northern California: Bull. Seismol. Soc. Am., v. 98, no. 2, p. 950-968.

Denison, R. E., 1981, Basement rocks in northeastern Oklahoma: Oklahoma Geological Survey Circular, v. 84, p. 83.

Dycus, M., 2013, Structural Characterization of the Wilzetta Fault Zone: Lincoln, Pottawatomie, and Creek Counties, Oklahoma [M.S. Thesis]: University of Tulsa.

Elebiju, O. O., Maston, S., Keller, G. R., and Marfurt, K. J., 2011, Integrated Geophysical Studies of the Basement Structures, Mississippi Chert, and the Arbuckle Group of Osage County, Oklahoma: AAPG Bulletin, v. 95, no. 3, p. 371-393.

Havskov, J., and Ottemöller, L., 1999, SeisAn Earthquake Analysis Software: Seism. Res. Lett., v. 70, no. 5, p. 532-534.

Holland, A. A., 2013, Optimal fault orientations within Oklahoma: Seismol. Res. Lett, v. 84, p. 876-890.

Huffman, G. G., 1958, Geology of the south and west flanks of the Ozark uplift, northeastern Oklahoma: Oklahoma Geological Survey Bulletin, v. 77, p. 281.

Johnson, K. S., 2008, Geologic History of Oklahoma: OKlahoma Geological Survey Educational Publications, v. 9, p. 4.

Joseph, L. R., 1986, Subsurface Analysis,"Cherokee" Group (Des Monesian), Portions of Lincoln, Pottawatomie, Seminole, and Okfuskee Counties, Oklahoma: Shale Shaker, v. 37, p. 43.

Kennett, B. L. N., and Hilst, R. D. v. d., 1996, Using a Synthetic Continental Array to Study the Earth's Interior: Journal Physics of the Earth, v. 44, p. 669-674.

Keranen, K. M., Savage, H. M., Abers, G. A., and Cochran, E. S., 2013, Potentially induced earthquakes in Oklahoma, USA: Links between wastewater injection and the 2011 Mw 5.7 earthquake sequence: Geology, v. 41, no. 6, p. 699-702.

Keranen, K. M., Weingarten, M., Abers, G. A., Bekins, B. A., and Ge, S., 2014, Sharp increase in central Oklahoma seismicity since 2008 induced by massive wastewater injection: Science, v. 345, no. 6195, p. 448-451.

Kissing, E., Ellsworth, W. L., Eberhart-Phillips, D., and Kradolfer, U., 1994, Initial reference models in local earthquake tomography: J. Geoph. Res., v. 99, no. B10, p. 19635–19646.

Kisvarsanyi, E. B., 1990, General features of the St. Francois and Spavinaw granite-rhyolite terranes and the Precambrian metallogenic region of Southeast Missouri: USGS Bulletin, no. 1932, p. 48-57.

Lévêque, J., Rivera, L., and Witlinger, G., 1993, On the use of the checker-board test to access the resolution of tomographic inversions Geophys. J. Int, v. 115, p. 313-318.

Lomax, A., Virieux, J., Volant, P., and Berge-Thierry, C., 2000, Probablistic Earthquake Location in 3D and Layered Models, *in* Thurber, C. H., Raabinowitx, N., ed., Advances in Seismic Event Location: Boston, MA, Kluwer Academic Publishers, p. 101-134.

Luza, K. V., and Lawson, J. E., 1983, Seismicity and Tectonic Relationships of the Nemaha Uplift, part V (final report): Oklahoma Geological Survey Open File Report, v. OF1-83, p. 115p.

Mitchell, B. J., and Landisman, M., 1970, interpretation of a Crustal Section across Oklahoma: GSA Bulletin, v. 81, p. 2647-2656.

Northcutt, R. A., and Campbell, J. A., 1995, Geologic Provinces of Oklahoma: Oklahoma Geological Survey Open File Report, v. OF5-95.

Rawlingson, N., Reading, A. M., and Kennett, B. L. N., 2006, Lithospheric structure of Tasmania from a novel form of teleseismic tomography: J. Geoph. Res., v. 111, no. B02301, p. 1-21.

Sumy, D. F., Cochran, E. S., Keranen, K. M., Wei, M., and Abers, G. A., 2014, Observations of Static Coulomb Stress Triggering of the November 2011 M5.7 Oklahoma Earthquake Sequence: J. Geoph. Res., v. 119, no. 3, p. 1904-1923.

Tichelaar, B. W., and Ruff, L. J., 1989, How good are our best models? Jackknifing, bootstrapping, and earthquake depth: Eos, v. 70, no. 20, p. 593-606.

Toelle, B., Sitchler, J., and Pfannensteil, R., 2008, Pannotian Breakup (Iapetan Opening) Features In Central Oklahoma, 2008 SEG Annual Meeting: Las Vegas, SEG.

Tryggvason, E., and Qualls, B. R., 1967, Seismic Refraction Measurements of Crustal Structure in Oklahoma: J. Geoph. Res., v. 72, no. 14, p. 3738-3740.

van der Elst, N. J., Savage, H. M., Keranen, K. M., and Abers, G. A., 2013, Enhanced Remote Earthquake Triggering at Fluid-Injection Sites in the Midwestern United States: Science, v. 341, p. 164-167.

Way, H. S. K., 1983, Structural Study of the Hunton Lime of the Wilzetta Field, T12-13N, R5E, Lincoln County, Oklahoma, Pertaining to the Exploration for Hydrocarbons [M.S. Thesis]: Oklahoma State University, 80 p.